

A finite strain model for fiber angle plasticity of textile fabrics based on isogeometric shell finite elements

Thang X. Duong^a and Roger A. Sauer^{b,c,d*}

^a*Institute of Engineering Mechanics and Structural Analysis, University of the Bundeswehr Munich, 85577 Neubiberg, Germany*

^b*Institute for Structural Mechanics, Ruhr University Bochum, 44801 Bochum, Germany*

^c*Department of Structural Mechanics, Gdańsk University of Technology, 80-233 Gdańsk, Poland*

^d*Mechanical Engineering, Indian Institute of Technology Guwahati, Assam 781039, India*

Abstract: This work presents a shear elastoplasticity model for textile fabrics within the theoretical framework of anisotropic Kirchhoff-Love shells with bending of embedded fibers proposed by Duong et al. (2023). The plasticity model aims at capturing the rotational inter-ply frictional sliding between fiber families in textile composites undergoing large deformation. Such effects are usually dominant in dry textile fabrics such as woven and non-crimp fabrics. The model explicitly uses relative angles between fiber families as strain measures for the kinematics. The plasticity model is formulated directly with surface invariants without resorting to thickness integration. Motivated by experimental observations from the picture frame test, a yield function is proposed with isotropic hardening and a simple evolution equation. A classical return mapping algorithm is employed to solve the elastoplastic problem within the isogeometric finite shell element formulation of Duong et al. (2022). The verification of the implementation is facilitated by the analytical solution for the picture frame test. The proposed plasticity model is calibrated from the picture frame test and is then validated by the bias extension test, considering available experimental data for different samples from the literature. Good agreement between model prediction and experimental data is obtained. Finally, the applicability of the elastoplasticity model to 3D shell problems is demonstrated.

Keywords: anisotropic bending; fiber composites; in-plane bending; Kirchhoff-Love shells; elastoplasticity; textiles

1 Introduction

This work is concerned with dry textile fabric sheets that are formed by two (or more) families of fiber bundles – called warp and weft yarns, which are loosely linked together by weaving (resulting in woven fabrics) or by stitching (resulting in non-crimp fabrics). These fabric structures are widely used in the automotive, marine and aeronautic industry due to their high specific stiffness-to-weight ratio.

Our present contribution aims at formulating a general shear elastoplasticity model for such dry textile fabrics in the framework of nonlinear Kirchhoff-Love shells and rotation-free isogeometric finite element discretization. In particular, we focus on the angle plasticity of woven fabrics, which is the plasticity induced by rotational sliding between warp and weft yarns when the fabric undergoes deformation. Our model assumes that the plastic shear behavior of the fabric is governed by two main mechanisms:

*corresponding author, email: roger.sauer@rub.de

At small deformation, friction between warp and weft yarns is the dominant mechanism, while at large deformation, the fabric behavior is dominated by *locking* between tows (i.e. warp and weft yarns) (Cao et al., 2008). Locking denotes the state when the rotation of tows becomes restricted due to their in-plane compression.

In order to formulate constitutive models for shells (including elastoplasticity), two main approaches are usually distinguished in the literature:

The first is characterized by *numerical thickness integration* that numerically reduces (or projects) the underlying 3D continuum to a 2D one. Examples of this type are found, among others, by Stanley (1985); Brank et al. (1997); Wagner and Gruttmann (2005); Kim and Lomboy (2006); Cortivo et al. (2009); Kiendl et al. (2015); Liu et al. (2022). This approach uses existing 3D constitutive models and obtains their surface counterparts by numerical thickness integration. The integrand is usually the 3D stress function, but the method extends to other quantities, such as strain, energy and algorithms. The *numerical thickness integration* approach has been widely used for shells, since the computational procedure is straightforward, as long as the underlying 3D material model exists. An example is the thickness integration of the classical J_2 -plasticity model with isotropic hardening, see e.g. Simo and Hughes (2006). The method has also been applied to anisotropic large strain elastoplasticity (Schieck et al., 1999) as well as viscoplasticity (Sansour and Wagner, 2001). In the field of isogeometric Kirchhoff-Love shells, the work of Ambati et al. (2018) is the first application of a rotation free shell formulation to elastoplasticity. This was then followed by Huynh et al. (2020) and Alaydin et al. (2021).

The second is a *direct surface* approach that avoids numerical integration. Now the shell equations are directly formulated (or theoretically derived) in surface form, which allows to make the computational formulation more efficient. The approach is also referred to the *stress-resultant* approach in the literature, see e.g. Simo and Kennedy (1992). In order to obtain this, various modeling techniques can be used. Depending on the treatment of the thickness, one can further subdivide the *direct surface* approach into *analytical thickness integration* and *surface invariant-based* approaches.

In the *analytical thickness integration* approach, the stress resultant is obtained by (exact or approximate) analytical integration over the thickness of an existing 3D constitutive model, or the stress resultant is proposed directly in surface form such that the 3D model is recovered (exactly or approximately). Therefore, this approach can usually be distinguished by the thickness variable that is considered as an extrinsic parameter (i.e. a geometrical quantity that is not part of the material properties). Examples are found, among others, by Simo and Fox (1989); Kiendl et al. (2015) for hyperelasticity, and Simo and Kennedy (1992); Skallerud and Haugen (1999); Skallerud et al. (2001); Zeng et al. (2001); Dujc and Brank (2012); Magisano and Corrado (2023) for elastoplasticity. In particular, Simo and Kennedy (1992) proposed an *analytical thickness integration* model for J_2 -plasticity, which is generalized from the two-yield-surface model of Shapiro (1961) for kinematic and isotropic hardening. The yield surface is expressed in terms of the stress resultants, which in turn are obtained from an analytical thickness integration. It should be noted that the exact stress and stress couple resultant that result from such an integration are quite complicated, which is shown e.g. by Duong et al. (2017) cf. Eq. (64). Thus, when applied to elastoplasticity even with simple J_2 -plasticity, a highly complicating expression for the stress resultants is obtained (Simo and Kennedy, 1992).

The *surface invariant-based* approach can also be categorized into the *direct surface* approach. However, in contrast to the *analytical thickness integration*, the stress resultant is usually not constructed from an existing 3D material model. Instead, it is derived from a surface energy density function that is constructed directly in terms of surface invariants without resorting to a thickness variable. Examples of this type are the shell models of Canham (1970) and Helfrich

(1973). Facilitated by the representation theorem (Rivlin and Rideal, 1949), the invariant-based formalism – see e.g. Spencer (1984); Rubin and Jabareen (2008); Melnik et al. (2018) – usually plays an important role in reducing the modeling complexity. From another perspective, *surface-invariant-based* models are usually distinguished by considering the thickness variable as an intrinsic parameter of the material model (i.e. the thickness variable becomes part of the material properties).

In applications of the approaches discussed above, the *thickness integration* approach (either numerical or analytical) usually find its advantages when the shell thickness can be well-defined and well-measured, like for a metal sheet at engineering scale, so that thickness integration can be performed for a 3D material model. The *surface invariant-based* approach, on the other hand, finds its advantage in shell structures where the shell thickness is not well-defined to be measured accurately. An example are lipid bilayers that behave like a liquid in-plane and like a solid out-of-plane (Zimmerberg and Kozlov, 2006). An other example is graphene, where the shell thickness is at the atomic scale with bending resistance induced by electromagnetic interaction forces (Lu et al., 2009). In particular for dry textile shells as considered in this work, the thickness is usually not well-defined or measured accurately either, since the thickness scale is equivalent to the scale of a yarn, which consists of fibers only loosely compacted (Allaoui et al., 2012). Further, the dominant mechanism for angle plasticity is frictional contact between yarns. For each neighboring pair of fiber families, there is a yarn-yarn contact interface along the thickness direction. Accurately accounting for all contact conditions in the thickness integration can become complicating.

Apart from using *direct surface* material models that avoid numerical thickness integration, the efficiency in shell computations can be further improved by using Kirchhoff-Love shell formulations based on rotation-free isogeometric discretization (Hughes et al., 2005) that requires only three displacement degrees of freedoms per control point. Such a shell formulation was first proposed by Kiendl et al. (2009) and extended to the general nonlinear setting by Kiendl et al. (2015). Its efficiency when combined with *direct surface* material models has been demonstrated for various types of nonlinear shells, such as engineering shells (Kiendl et al., 2015; Duong et al., 2017), liquid shells (Sauer et al., 2017; Auddya et al., 2021), biological shells (Tepole et al., 2015; Roohbakhshan and Sauer, 2017), graphene (Ghaffari et al., 2018; Mokhalingam et al., 2024), phase transitions on shells (Zimmermann et al., 2019; Paul et al., 2020), and textiles (Duong et al., 2022).

In shell formulations for dry textile fabrics, it is required to account for in-plane bending of embedded fibers as it becomes significant in certain loading scenarios (Ferretti et al., 2014; Madeo et al., 2016; Boisse et al., 2017; Barbagallo et al., 2017). In this case, a gradient shell theory can be used, see e.g. Spencer and Soldatos (2007); Steigmann (2012); dell’Isola and Steigmann (2015); Steigmann (2018). Corresponding gradient-theory-based computational formulations can be found in e.g. Asmanoglo and Menzel (2017); Balabanov et al. (2019); Schulte et al. (2020); Witt et al. (2021). Alternatively to gradient theory, in-plane bending of embedded fibers can also be captured by Kirchhoff-Love shell theory extended to the geodesic curvature of embedded fibers. As demonstrated by Duong et al. (2023), such a generalized theory can be formulated directly from Kirchhoff-Love assumptions similarly to out-of-plane bending, without resorting to a general gradient shell theory. Its rotation-free isogeometric discretization and an efficient implementation was detailed in Duong et al. (2022). It is worth to mention here, that despite the additional kinematics, no extra degrees of freedom are required beyond the three displacement degrees of freedom in standard rotation-free shell formulations.

For finite element computations of textile fabrics where dissipation is not of interest, hyperelasticity is sufficient and more efficient. Examples are given, among others by Aimène et al. (2010);

Charmetant et al. (2012); Peng et al. (2013); Khiêm et al. (2018); Bussetta and Correia (2018); Li et al. (2023); Schäfer et al. (2023); Schäfer et al. (2024) and references therein. However, elastoplasticity is a more realistic behavior of textile fabrics. In this context, the first *surface invariant-based* elastoplasticity model was proposed by Denis et al. (2018) for 2D plane problems. Their model considers two fiber families with an initial relative angle of 90 degrees and is based on a fractional derivative model with 20 parameters for both kinematic and isotropic hardening. It uses nested yield surfaces in order to account for the asymptotic paths of unloading curves observed in their cyclic load experiments for carbon fabrics. Recently, Khiêm et al. (2024) propose a *surface invariant-based* model, which is formulated within a gradient damage (i.e. non-local) model of a 3D membrane based on the analytical averaging framework of Khiêm and Itskov (2016). It is capable of capturing the elastoplasticity of textile membranes¹ with only 7 physical constants.

In this contribution, we propose an angle elastoplasticity model directly in terms of surface invariants for textiles modeled by the (anisotropic) Kirchhoff-Love shell formulation of Duong et al. (2023). The proposed model has no limitation on the number of fiber families and initial angle between them. In order to obtain a simple but still applicable model for loading-unloading computations, we focus on reproducing the isotropic hardening observed in the shear behavior of fabrics. To the best of our knowledge, this is the first time such an elastoplasticity model is formulated and applied to an isogeometric shell formulation.

Our model is a *surface invariant-based* formulation. It uses surface invariants induced from fiber angles and proposes a yield function with isotropic hardening in terms of these invariants. The expression of the yield function uses 7 physical constants in order to capture the three deformation phases usually observed in the shear response of woven fabrics. Since we formulate the direct surface model based on invariants, only one (scalar) internal variable appears in the model. It can be shown that the adopted surface invariants are induced from strain tensors of the first displacement gradient, and correspond to a multiplicative split of the surface deformation gradient \mathbf{F} into elastic and plastic parts, \mathbf{F}_e and \mathbf{F}_p (Sauer et al., 2019). Unlike classical 3D isotropic plasticity where $\det \mathbf{F}_p = 1$, the plastic deformation in our formulation assumes no length change in fiber direction, which is a characteristic of many deforming textiles.

For the purpose of verifying finite element implementations, we further provide an analytical solution of the proposed model.

In summary, our contribution contains the following novelties and merits:

- It proposes a new shear elastoplasticity model for textile fabrics
- It has no limitation on the number of fiber families and the initial angles between them.
- Its strain energy is directly formulated in surface form without any thickness integration.
- It is based explicitly on the relative fiber angles and their elastoplastic split.
- It proposes a yield function with isotropic hardening for dry textile fabrics.
- It contains the analytical solution for elastoplasticity in the picture frame test.
- It contains model verification, calibration, and validation of the proposed model.

The remaining sections are organized as follows: Sec. 2 first summarizes the description of surface deformation with embedded fibers from Duong et al. (2023). It then presents different angle strain measures for the proposed angle plasticity model. Sec. 3 summarizes the weak form and residual vector of the isogeometric finite element formulation of Duong et al. (2022). Sec. 4

¹where out-of-plane bending resistance is neglected.

extends the simple constitutive fabric model of [Duong et al. \(2023\)](#) to fiber angle plasticity. Sec. 5 presents the proposed angle elastoplasticity model in detail. In Sec. 6, the finite element implementation is verified by the analytical solution for the elastoplastic picture frame test, and the influence of model parameters is illustrated. Sec. 7 then discusses the calibration and validation of the proposed model. A three dimensional example is shown in Sec. 8. Finally, Sec. 9 concludes the paper.

2 Surface deformation with embedded fibers

This section first introduces essential geometrical objects used to describe thin shells with embedded fibers under large deformations within the general theory for anisotropic Kirchhoff-Love shells of [Duong et al. \(2023\)](#). A multiplicative split of the deformation gradient suitable for angle elastoplasticity is then presented.

2.1 Surface description

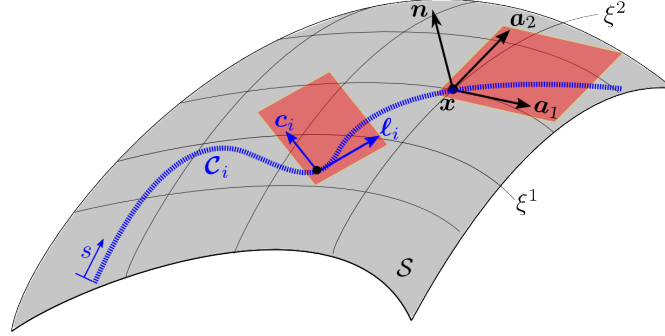


Figure 1: Shell surface \mathcal{S} with an embedded fiber bundle along curve \mathcal{C} ([Duong et al., 2023](#)). Multiple fiber families are distinguished by index $i = 1, 2, 3, \dots, n_f$. The red planes illustrate tangent planes.

A mathematical surface \mathcal{S} representing the mid-surface of the shell in \mathbb{R}^3 at any time t is defined by the one-to-one mapping from a point (ξ^1, ξ^2) in 2D parameter space \mathcal{P} to the point $\mathbf{x} \in \mathcal{S}$ as (see Fig. 1)

$$\mathbf{x} = \mathbf{x}(\xi^\alpha, t). \quad (1)$$

The two tangent vectors at $\mathbf{x} \in \mathcal{S}$

$$\mathbf{a}_\alpha := \frac{\partial \mathbf{x}}{\partial \xi^\alpha} = \mathbf{x}_{,\alpha}, \quad (2)$$

with $\alpha = 1, 2$ define the unit normal vector

$$\mathbf{n} := \frac{\mathbf{a}_1 \times \mathbf{a}_2}{\|\mathbf{a}_1 \times \mathbf{a}_2\|}. \quad (3)$$

From these follow the components of the surface metric

$$a_{\alpha\beta} := \mathbf{a}_\alpha \cdot \mathbf{a}_\beta, \quad (4)$$

and the components of the out-of-plane surface curvature

$$b_{\alpha\beta} := \mathbf{n} \cdot \mathbf{a}_{\alpha,\beta} = -\mathbf{n}_{,\beta} \cdot \mathbf{a}_\alpha. \quad (5)$$

Here, the latter identity follows from $\mathbf{n} \cdot \mathbf{a}_\alpha = 0$. The contra-variant metric components

$$a^{\alpha\beta} := [a_{\alpha\beta}]^{-1}, \quad (6)$$

relate the dual tangent vectors \mathbf{a}^α to the tangent vectors \mathbf{a}_α by²

$$\mathbf{a}^\alpha = a^{\alpha\beta} \mathbf{a}_\beta, \quad (7)$$

which satisfies $\mathbf{a}^\alpha \cdot \mathbf{a}_\beta = \delta_\beta^\alpha$.

Note, that vectors $\mathbf{a}_{\alpha,\beta}$ appearing in (5) have both in-plane and out-of-plane components, i.e.

$$\mathbf{a}_{\alpha,\beta} = \Gamma_{\alpha\beta}^\gamma \mathbf{a}_\gamma + b_{\alpha\beta} \mathbf{n}, \quad (8)$$

where the in-plane components $\Gamma_{\alpha\beta}^\gamma := \mathbf{a}_{\alpha,\beta} \cdot \mathbf{a}^\gamma$ denote the so-called Christoffel symbols.

Further, a fiber family \mathcal{C} embedded in surface \mathcal{S} is characterized by its normalized fiber tangent vector $\boldsymbol{\ell} := \partial \mathbf{x} / \partial s$ with s denoting the parametric coordinate along \mathcal{C} , and by fiber director vector $\mathbf{c} := \mathbf{n} \times \boldsymbol{\ell}$, see Fig. 1. These vectors can be expressed in bases $\{\mathbf{a}^1, \mathbf{a}^2, \mathbf{n}\}$ and $\{\mathbf{a}_1, \mathbf{a}_2, \mathbf{n}\}$ as

$$\boldsymbol{\ell} = \ell_\alpha \mathbf{a}^\alpha = \ell^\alpha \mathbf{a}_\alpha, \quad (9)$$

$$\mathbf{c} = c_\alpha \mathbf{a}^\alpha = c^\alpha \mathbf{a}_\alpha. \quad (10)$$

For the sake of concise expressions, we further define the Christoffel symbols associated with directions \mathbf{c} and $\boldsymbol{\ell}$ as

$$\Gamma_{\alpha\beta}^c := \mathbf{c} \cdot \mathbf{a}_{\alpha,\beta} = c_\gamma \Gamma_{\alpha\beta}^\gamma, \quad \Gamma_{\alpha\beta}^\ell := \boldsymbol{\ell} \cdot \mathbf{a}_{\alpha,\beta} = \ell_\gamma \Gamma_{\alpha\beta}^\gamma. \quad (11)$$

Similarly to Eq. (5), the components of the (symmetric) in-plane fiber curvature tensor can be defined from the parametric derivatives of the fiber director, $\mathbf{c}_{,\alpha}$, as

$$\bar{b}_{\alpha\beta} := -\frac{1}{2}(\mathbf{c}_{,\alpha} \cdot \mathbf{a}_\beta + \mathbf{c}_{,\beta} \cdot \mathbf{a}_\alpha). \quad (12)$$

According to this, only the in-plane components of vectors $\mathbf{c}_{,\alpha}$ contribute to the in-plane fiber curvature tensor. We thus can rewrite Eq. (12) as

$$\bar{b}_{\alpha\beta} = -\frac{1}{2}(\bar{\mathbf{c}}_{,\alpha} \cdot \mathbf{a}_\beta + \bar{\mathbf{c}}_{,\beta} \cdot \mathbf{a}_\alpha) = -\frac{1}{2}(c_{\alpha;\beta} + c_{\beta;\alpha}), \quad (13)$$

where the semicolon denotes the covariant derivative, and where

$$\bar{\mathbf{c}}_{,\alpha} := (\mathbf{a}_\beta \otimes \mathbf{a}^\beta) \mathbf{c}_{,\alpha} \quad (14)$$

denote the projection of vectors $\mathbf{c}_{,\alpha}$ onto the current tangent plane. As a result, vectors $\bar{\mathbf{c}}_{,\alpha}$ only have in-plane components, i.e.

$$\bar{\mathbf{c}}_{,\alpha} = c_{;\alpha}^\beta \mathbf{a}_\beta = c_{\beta;\alpha} \mathbf{a}^\beta. \quad (15)$$

According to Duong et al. (2023), the curvature tensors (5) and (12) can induce useful invariants to measure curvatures of embedded fiber such as

$$\begin{aligned} \kappa_n &:= b_{\alpha\beta} \ell^{\alpha\beta}, \quad \text{with } \ell^{\alpha\beta} := \ell^\alpha \ell^\beta, \\ \tau_g &:= b_{\alpha\beta} \ell^\alpha c^\beta, \\ \kappa_g &:= \bar{b}_{\alpha\beta} \ell^{\alpha\beta}. \end{aligned} \quad (16)$$

They denote the normal curvature, geodesic torsion, and geodesic curvature of the embedded fiber, respectively. Note, that only the magnitude of the curvature measures (16) is strictly invariant, while their sign depends on the direction of vectors \mathbf{n} , $\boldsymbol{\ell}$, and/or \mathbf{c} .

²In this paper, the summation convention is applied to repeated Greek indices taking values from 1 to 2.

2.2 Surface deformation

In order to measure shell deformations, we distinguish between the reference configuration \mathcal{S}_0 at time $t = 0$ and the current configuration \mathcal{S} at time $t > 0$.

The geometrical objects of Sec. 2.1 are defined analogously on \mathcal{S}_0 using uppercase (or 0-indexed) symbols, giving tangent vectors \mathbf{A}_α , normal vector \mathbf{N} , metric components $A_{\alpha\beta}$, out-of-plane curvature tensor $B_{\alpha\beta}$, in-plane curvature tensor $\bar{B}_{\alpha\beta}$, normalized fiber direction $\mathbf{L} = L^\alpha \mathbf{A}_\alpha = L_\alpha \mathbf{A}^\alpha$, and fiber director $\mathbf{c}_0 = c_\alpha^0 \mathbf{A}^\alpha$.

The in-plane surface deformation is characterized by the surface deformation gradient

$$\mathbf{F} := \mathbf{a}_\alpha \otimes \mathbf{A}^\alpha . \quad (17)$$

It is used to define the right Cauchy-Green surface tensor

$$\mathbf{C} := \mathbf{F}^\top \mathbf{F} = a_{\alpha\beta} \mathbf{A}^\alpha \otimes \mathbf{A}^\beta , \quad (18)$$

as well as the Green-Lagrange surface strain tensor $\mathbf{E} := (\mathbf{C} - \mathbf{I})/2$, that has the components

$$E_{\alpha\beta} := \frac{1}{2} (a_{\alpha\beta} - A_{\alpha\beta}) . \quad (19)$$

Further, \mathbf{F} pushes forward the fiber direction according to

$$\lambda \boldsymbol{\ell} = \mathbf{F} \mathbf{L} , \quad (20)$$

where $\lambda = \|\mathbf{F} \mathbf{L}\|$ denotes the fiber stretch.

The out-of-plane bending deformation is characterized by the relative surface curvature

$$K_{\alpha\beta} := b_{\alpha\beta} - B_{\alpha\beta} , \quad (21)$$

and similarly the in-plane fiber bending deformation is characterized by the relative in-plane curvature

$$\bar{K}_{\alpha\beta} := \bar{b}_{\alpha\beta} - \bar{B}_{\alpha\beta} , \quad (22)$$

where components $\bar{b}_{\alpha\beta}$ can be computed from definition (12) with $c_{\beta;\alpha}$ expressed in terms of deformation map (20) as

$$\begin{aligned} c_{\beta;\alpha} &= -\ell_\beta (\lambda^{-1} c_\gamma L_{,\alpha}^\gamma + \ell^\gamma \Gamma_{\gamma\alpha}^c) , \\ c_{;\alpha}^\beta &= -\ell^\beta (\lambda^{-1} c_\gamma L_{,\alpha}^\gamma + \ell^\gamma \Gamma_{\gamma\alpha}^c) . \end{aligned} \quad (23)$$

Note that for multiple fiber families, fiber-related quantities – such as Eq. (20), (22) and (23) – are defined separately for each fiber family.

With strains measures (18), (21) and (22), various strain invariants useful for the construction of material models can be induced. For example (Duong et al., 2023)

$$\begin{aligned} I_1 &:= A^{\alpha\beta} a_{\alpha\beta} , \\ \Lambda_i &:= a_{\alpha\beta} L_i^{\alpha\beta} , \\ T_g &:= b_{\alpha\beta} c_0^\alpha L^\beta - \tau_g^0 , \\ K_n &:= \kappa_n \lambda^2 - \kappa_n^0 , \\ K_g &:= \kappa_g \lambda^2 - \kappa_g^0 , \end{aligned} \quad (24)$$

are the surface shear measure of \mathcal{S} , the fiber stretch, the nominal change in geodesic fiber torsion, normal fiber curvature, and geodesic fiber curvature, respectively.

2.3 Angle strain measures for shear elastoplasticity

This section presents angle strain measures suitable for angle elastoplasticity of textile materials under large deformations. It also shows, that various measures for relative fiber angles are invariants that can be properly induced from strain tensors of the displacement gradient.

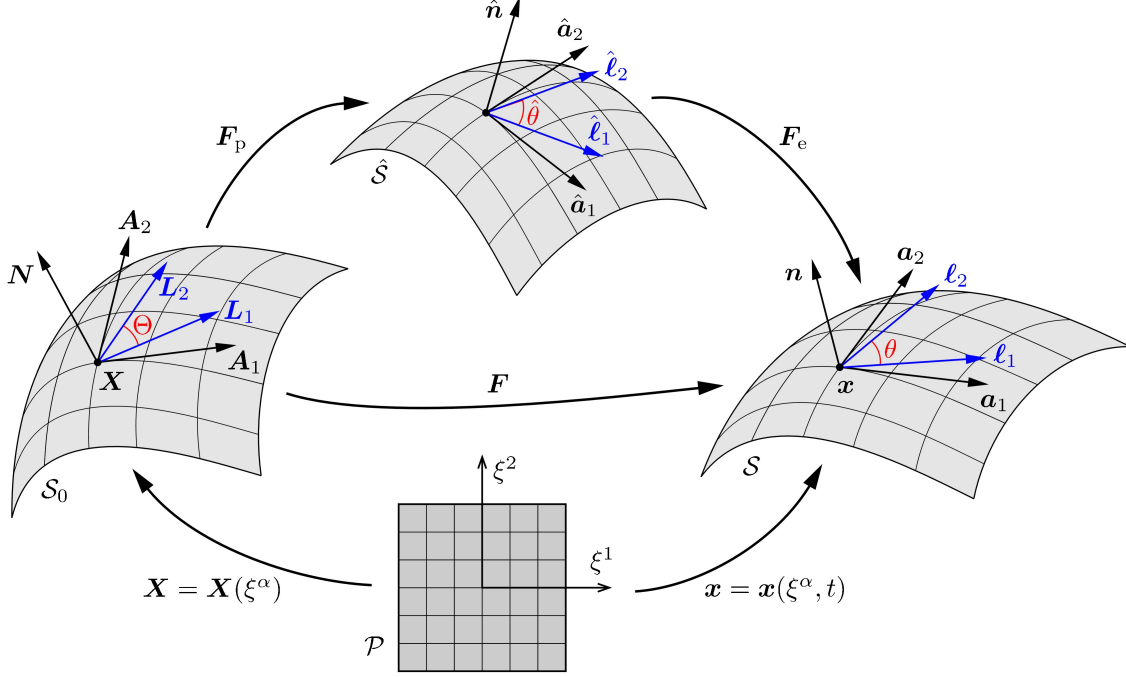


Figure 2: Split of the surface deformation into elastic and plastic parts (Sauer et al., 2019). This introduces the intermediate configuration $\hat{\mathcal{S}}$ between reference and current configurations \mathcal{S}_0 and \mathcal{S} . The geometrical objects of Sec. 2.1 are defined likewise in the three configurations. In particular, fiber angle measures $\Theta_{12} := \mathbf{L}_1 \cdot \mathbf{L}_2 = \cos \Theta$, $\theta_{12} := \boldsymbol{\ell}_1 \cdot \boldsymbol{\ell}_2 = \cos \theta$ and $\hat{\theta}_{12} := \hat{\boldsymbol{\ell}}_1 \cdot \hat{\boldsymbol{\ell}}_2 = \cos \hat{\theta}$ are defined here for a pair of two fiber families \mathcal{C}_1 and \mathcal{C}_2 .

To this end, an intermediate (fictitious) configuration $\hat{\mathcal{S}}$ is introduced following Sauer et al. (2019), see Fig. 2. The geometrical objects of Sec. 2.1 are defined analogously on $\hat{\mathcal{S}}$ using a hat, giving tangent vectors $\hat{\mathbf{a}}_\alpha$, normal vector $\hat{\mathbf{n}}$, and metric components $\hat{a}_{\alpha\beta}$. With this, the deformation gradient (17) is split into plastic and elastic parts as

$$\mathbf{F} = \mathbf{F}_e \mathbf{F}_p, \quad (25)$$

where

$$\mathbf{F}_p := \hat{\mathbf{a}}_\alpha \otimes \mathbf{A}^\alpha, \quad (26)$$

$$\mathbf{F}_e := \mathbf{a}_\alpha \otimes \hat{\mathbf{a}}^\alpha. \quad (27)$$

The area stretch $J := \det_s \mathbf{F}$ can then be expressed as

$$J = J_e J_p, \quad \text{where } J_e := \det_s \mathbf{F}_e \quad \text{and} \quad J_p := \det_s \mathbf{F}_p. \quad (28)$$

In order to characterize angle plasticity, we consider a pair of fiber families – indexed by 1 and 2.³ Under deformations, the directions of fiber family \mathcal{C}_i (with $i = 1, 2$) in configurations \mathcal{S}_0 ,

³For multiple pairs of fiber families in \mathcal{S} , the kinematics in this section is simply replicated for each pair.

$\hat{\mathcal{S}}$, and \mathcal{S} are \mathbf{L}_i , $\hat{\boldsymbol{\ell}}_i$, and $\boldsymbol{\ell}_i$, respectively. The relative angles cosines between fibers i and j are defined by

$$\Theta_{ij} := \mathbf{L}_i \cdot \mathbf{L}_j , \quad (29)$$

$$\hat{\theta}_{ij} := \hat{\boldsymbol{\ell}}_i \cdot \hat{\boldsymbol{\ell}}_j , \quad (30)$$

$$\theta_{ij} := \boldsymbol{\ell}_i \cdot \boldsymbol{\ell}_j \quad (31)$$

in configurations \mathcal{S}_0 , $\hat{\mathcal{S}}$, and \mathcal{S} , respectively. Note that in these equations $\Theta_{ii} = \hat{\theta}_{ii} = \theta_{ii} = 1$ (no sum on i), since vectors $\|\mathbf{L}_i\| = \|\hat{\boldsymbol{\ell}}_i\| = \|\boldsymbol{\ell}_i\| = 1$. Therefore, the mixed components become $\Theta_{12} = \cos \Theta$, $\hat{\theta}_{12} = \cos \hat{\theta}$, and $\theta_{12} = \cos \theta$, where Θ , $\hat{\theta}$, and θ denote the corresponding relative angles between fiber family 1 and 2 in configurations \mathcal{S}_0 , $\hat{\mathcal{S}}$, and \mathcal{S} , respectively. Further, Eqs. (29)-(31) induce surface metrics that can be arranged in matrix form, e.g.

$$[\Theta_{ij}] = \begin{bmatrix} 1 & \Theta_{12} \\ \Theta_{12} & 1 \end{bmatrix} . \quad (32)$$

For the angle plasticity model proposed in this work, we employ the following measures of the relative fiber angle change during deformation

$$\phi := \theta_{12} - \Theta_{12} , \quad (33)$$

$$\phi_e := \theta_{12} - \hat{\theta}_{12} , \quad (34)$$

$$\phi_p := \hat{\theta}_{12} - \Theta_{12} , \quad (35)$$

that satisfy the additive split

$$\phi = \phi_e + \phi_p . \quad (36)$$

Further, we pick deformation gradient \mathbf{F}_p such that fiber lengths are preserved in configuration $\hat{\mathcal{S}}$. Namely,

$$\mathbf{F}_p = \hat{\boldsymbol{\ell}}_i \otimes \mathbf{L}^i , \quad (37)$$

where \mathbf{L}^i is the fiber direction vector dual to \mathbf{L}_i in \mathcal{S}_0 , defined by

$$\mathbf{L}^i = \Theta^{ij} \mathbf{L}_j , \quad \text{with} \quad [\Theta^{ij}] := [\Theta_{ij}]^{-1} . \quad (38)$$

By comparing Eq. (37) and (26) we obtain an expression for $\hat{\mathbf{a}}_\alpha$ in terms of the fiber directions, i.e.

$$\hat{\mathbf{a}}_\alpha = (\mathbf{L}^i \cdot \mathbf{A}_\alpha) \hat{\boldsymbol{\ell}}_i = \mathbf{F}_p \mathbf{A}_\alpha . \quad (39)$$

In Eqs. (37)-(39), summation is implied on repeated Latin indices taking value from 1 to 2.

Remark 2.1: The angle strain measures ϕ , ϕ_e and ϕ_p defined from Eq. (33)-(35) are invariants that can be properly induced from strain tensors related to the displacement gradient. This is shown in Appendix A. It should be noted, that similarly to the curvature measures (16), only the magnitude of these measures is invariant in a strict sense, since their sign still depends on the direction of the fiber directions, which is exchangeable. However, it can easily be shown that (both the sign and magnitude of) the measures ϕ , ϕ_e and ϕ_p are frame invariant under superimposed rigid body motions of the shell surface.

2.4 Variations of kinematical quantities

We consider a variation of the surface deformation, denoted $\delta \mathbf{x}$, which causes variations in \mathbf{a}_α , denoted $\delta \mathbf{a}_\alpha = \delta \mathbf{x}_{,\alpha}$.

The variation of the kinematical quantities in Eqs. (19), (21) and (22) requires $\delta a_{\alpha\beta}$, $\delta b_{\alpha\beta}$ and $\delta \bar{b}_{\alpha\beta}$. They are given by (Sauer and Duong, 2017; Duong et al., 2023)

$$\begin{aligned}\delta a_{\alpha\beta} &= \delta \mathbf{a}_\alpha \cdot \mathbf{a}_\beta + \mathbf{a}_\alpha \cdot \delta \mathbf{a}_\beta, \\ \delta b_{\alpha\beta} &= \mathbf{n} \cdot \delta \mathbf{d}_{\alpha\beta}, \quad \text{with} \quad \delta \mathbf{d}_{\alpha\beta} := \delta \mathbf{a}_{\alpha,\beta} - \Gamma_{\alpha\beta}^\gamma \delta \mathbf{a}_\gamma, \\ \bar{M}_0^{\alpha\beta} \delta \bar{b}_{\alpha\beta} &= -\bar{M}_0^{\alpha\beta} (\delta \mathbf{a}_\alpha \cdot \bar{\mathbf{c}}_{,\beta} + \mathbf{a}_\alpha \cdot \delta \bar{\mathbf{c}}_{,\beta}),\end{aligned}\tag{40}$$

where the last equation holds for any symmetric tensor $\bar{M}_0^{\alpha\beta}$.

The variation $\delta \phi$ follows from Eqs. (33), (31) and (9) as (Duong et al., 2023)

$$\delta \phi = \delta \theta_{12} = g_{12}^{\alpha\beta} \delta a_{\alpha\beta},\tag{41}$$

where we have defined

$$g_{12}^{\alpha\beta} := \frac{1}{2} (\ell_1^\alpha \ell_2^\beta + \ell_1^\beta \ell_2^\alpha) - \frac{\theta_{12}}{2} (\ell_1^{\alpha\beta} + \ell_2^{\alpha\beta}), \quad \text{with} \quad \ell_i^{\alpha\beta} := \ell_i^\alpha \ell_i^\beta \quad (\text{no sum on } i),\tag{42}$$

Furthermore, the linearization of $g_{12}^{\alpha\beta}$ can also be found in Duong et al. (2023), as

$$\Delta g_{12}^{\alpha\beta} = g_{12}^{\alpha\beta\gamma\delta} \Delta a_{\gamma\delta},\tag{43}$$

with

$$g_{12}^{\alpha\beta\gamma\delta} := \frac{\partial g_{12}^{\alpha\beta}}{\partial a_{\gamma\delta}} = -(\ell_1^\alpha \ell_2^\beta)^{\text{sym}} \frac{1}{2} (\ell_1^{\gamma\delta} + \ell_2^{\gamma\delta}) - \frac{1}{2} (\ell_1^{\alpha\beta} + \ell_2^{\alpha\beta}) g_{12}^{\gamma\delta} + \frac{\theta_{12}}{2} (\ell_1^{\alpha\beta} \ell_1^{\gamma\delta} + \ell_2^{\alpha\beta} \ell_2^{\gamma\delta}).\tag{44}$$

3 Finite element formulation

This section summarizes the finite element formulation for Kirchhoff-Love shells with embedded fibers from Duong et al. (2023). Namely, the weak form, finite element force vectors, and the definition of the material tangents are recalled here. It should be noted that the form of these equations is unchanged for plastic deformations. Only the constitutive model changes as will be discussed in detail in Sec. 4.

3.1 Weak form

The shell is subjected to external body force \mathbf{f} , external boundary traction \mathbf{T} , external out-of-plane bending moment \mathbf{M} , and external in-plane fiber bending moment $\bar{\mathbf{M}}_i$. On the shell boundaries $\partial_u \mathcal{S}$ and $\partial_n \mathcal{S}$, displacements and rotations can be prescribed, respectively. For all $\delta \mathbf{x}$ within the set of kinematically admissible variations \mathcal{V} , the weak form follows from the principle of virtual work as (Duong et al., 2023)

$$G_{\text{in}} + G_{\text{int}} - G_{\text{ext}} = 0 \quad \forall \delta \mathbf{x} \in \mathcal{V},\tag{45}$$

where

$$\begin{aligned}
G_{\text{in}} &= \int_{S_0} \delta \mathbf{x} \cdot \rho_0 \dot{\mathbf{v}} \, dA , \\
G_{\text{int}} &= \frac{1}{2} \int_{S_0} \tau^{\alpha\beta} \delta a_{\alpha\beta} \, dA + \int_{S_0} M_0^{\alpha\beta} \delta b_{\alpha\beta} \, dA + \sum_{i=1}^{n_f} \int_{S_0} \bar{M}_{0i}^{\alpha\beta} \delta \bar{b}_{\alpha\beta}^i \, dA , \\
G_{\text{ext}} &= \int_S \delta \mathbf{x} \cdot \mathbf{f} \, da + \int_{\partial S} \delta \mathbf{x} \cdot \mathbf{T} \, ds + \int_{\partial S} \delta \mathbf{n} \cdot \mathbf{M} \, ds + \sum_{i=1}^{n_f} \int_{\partial S} \delta \mathbf{c}_i \cdot \bar{\mathbf{M}}_i \, ds .
\end{aligned} \tag{46}$$

Here, n_f , $\tau^{\alpha\beta}$, $M_0^{\alpha\beta}$, and $\bar{M}_{0i}^{\alpha\beta}$ are the number of fiber families, the components of the effective stress tensor, the nominal stress couple tensor associated with out-of-plane bending, and the nominal stress couple tensor associated with in-plane fiber bending, respectively.

From the linearization of internal virtual work (46.2) follows⁴

$$\begin{aligned}
\Delta G_{\text{int}} &= \int_{S_0} \left[c^{\alpha\beta\gamma\delta} \frac{1}{2} \delta a_{\alpha\beta} \frac{1}{2} \Delta a_{\gamma\delta} + d^{\alpha\beta\gamma\delta} \frac{1}{2} \delta a_{\alpha\beta} \Delta b_{\gamma\delta} + \bar{d}_i^{\alpha\beta\gamma\delta} \frac{1}{2} \delta a_{\alpha\beta} \Delta \bar{b}_{\gamma\delta}^i \right. \\
&+ e^{\alpha\beta\gamma\delta} \delta b_{\alpha\beta} \frac{1}{2} \Delta a_{\gamma\delta} + f^{\alpha\beta\gamma\delta} \delta b_{\alpha\beta} \Delta b_{\gamma\delta} + \bar{g}_i^{\alpha\beta\gamma\delta} \delta b_{\alpha\beta} \Delta \bar{b}_{\gamma\delta}^i \\
&+ \bar{e}_i^{\alpha\beta\gamma\delta} \delta \bar{b}_{\alpha\beta}^i \frac{1}{2} \Delta a_{\gamma\delta} + \bar{h}_i^{\alpha\beta\gamma\delta} \delta \bar{b}_{\alpha\beta}^i \Delta b_{\gamma\delta} + \bar{f}_{ij}^{\alpha\beta\gamma\delta} \delta \bar{b}_{\alpha\beta}^i \Delta \bar{b}_{\gamma\delta}^j \\
&\left. + \tau^{\alpha\beta} \frac{1}{2} \Delta \delta a_{\alpha\beta} + M_0^{\alpha\beta} \Delta \delta b_{\alpha\beta} + \bar{M}_{0i}^{\alpha\beta} \Delta \delta \bar{b}_{\alpha\beta}^i \right] dA ,
\end{aligned} \tag{47}$$

with the nine material tangents (Duong et al., 2023)

$$\begin{aligned}
c^{\alpha\beta\gamma\delta} &:= 2 \frac{\partial \tau^{\alpha\beta}}{\partial a_{\gamma\delta}} , & d^{\alpha\beta\gamma\delta} &:= \frac{\partial \tau^{\alpha\beta}}{\partial b_{\gamma\delta}} , & \bar{d}_i^{\alpha\beta\gamma\delta} &:= \frac{\partial \tau^{\alpha\beta}}{\partial \bar{b}_{\gamma\delta}^i} , \\
e^{\alpha\beta\gamma\delta} &:= 2 \frac{\partial M_0^{\alpha\beta}}{\partial a_{\gamma\delta}} , & f^{\alpha\beta\gamma\delta} &:= \frac{\partial M_0^{\alpha\beta}}{\partial b_{\gamma\delta}} , & \bar{g}_i^{\alpha\beta\gamma\delta} &:= \frac{\partial M_0^{\alpha\beta}}{\partial \bar{b}_{\gamma\delta}^i} , \\
\bar{e}_i^{\alpha\beta\gamma\delta} &:= 2 \frac{\partial \bar{M}_{0i}^{\alpha\beta}}{\partial a_{\gamma\delta}} , & \bar{h}_i^{\alpha\beta\gamma\delta} &:= \frac{\partial \bar{M}_{0i}^{\alpha\beta}}{\partial b_{\gamma\delta}} , & \bar{f}_{ij}^{\alpha\beta\gamma\delta} &:= \frac{\partial \bar{M}_{0i}^{\alpha\beta}}{\partial \bar{b}_{\gamma\delta}^j} .
\end{aligned} \tag{48}$$

3.2 FE discretization

As seen from weak form (46.2), the last two terms in the internal virtual work contain the virtual curvatures, which require at least C^1 -continuity across the surface. Here, we use an isogeometric discretization to fulfill this requirement. Since this discretization can provide a smooth and accurate description of the geometry, the curvature measures can be computed directly from the geometry. As a result, only three displacement dofs per control point are needed to properly describe the shell.

The undeformed element domain Ω_0^e and the deformed element domain Ω^e are interpolated as

$$\mathbf{X} = \mathbf{N}_e \mathbf{X}_e , \quad \text{and} \quad \mathbf{x} = \mathbf{N}_e \mathbf{x}_e , \tag{49}$$

where \mathbf{X}_e and \mathbf{x}_e are the initial and current positions of control points, respectively. The array

$$\mathbf{N}_e(\xi^\alpha) := [N_1 \mathbf{1}, N_2 \mathbf{1}, \dots, N_{n_e} \mathbf{1}] \tag{50}$$

⁴Apart from the Greek indices, summation is also implied on repeated fiber indices $i, j = 1 \dots n_f$.

contains the isogeometric shape functions (Borden et al., 2011) for each control point, and n_e is the number of control points defining the element.

From Eq. (49) follows the interpolation of other kinematical quantities, such as

$$\begin{aligned}\delta \mathbf{x} &= \mathbf{N}_e \delta \mathbf{x}_e \quad , & \mathbf{a}_{\alpha,\beta} &= \mathbf{N}_{e,\alpha\beta} \mathbf{x}_e \quad , \\ \mathbf{a}_\alpha &= \mathbf{N}_{e,\alpha} \mathbf{x}_e \quad , & \mathbf{a}_{\alpha;\beta} &= \mathbf{N}_{e;\alpha\beta} \mathbf{x}_e \quad , \\ \delta \mathbf{c}_\alpha &= \mathbf{N}_{e,\alpha} \delta \mathbf{x}_e \quad , & \delta \bar{\mathbf{c}}_{,\alpha} &= \mathbf{C}_{e,\alpha} \delta \mathbf{x}_e \quad .\end{aligned}\tag{51}$$

Here, we have defined the elemental arrays

$$\begin{aligned}\mathbf{N}_{e,\alpha} &:= [N_{1,\alpha} \mathbf{1}, N_{2,\alpha} \mathbf{1}, \dots, N_{n_e,\alpha} \mathbf{1}] \quad , \\ \mathbf{N}_{e,\alpha\beta} &:= [N_{1,\alpha\beta} \mathbf{1}, N_{2,\alpha\beta} \mathbf{1}, \dots, N_{n_e,\alpha\beta} \mathbf{1}] \quad , \\ \mathbf{N}_{e;\alpha\beta} &:= \mathbf{N}_{,\alpha\beta} - \Gamma_{\alpha\beta}^\gamma \mathbf{N}_{,\gamma} \quad , \\ \mathbf{C}_{e,\alpha} &:= [\mathcal{L}_\alpha^\gamma (\mathbf{I} - 2 \boldsymbol{\ell} \otimes \boldsymbol{\ell}) - \mathcal{C}_\alpha^\gamma \boldsymbol{\ell} \otimes \mathbf{c} - \mathcal{N}_\alpha^\gamma \boldsymbol{\ell} \otimes \mathbf{n}] \mathbf{N}_{,\gamma} - \ell^\gamma (\boldsymbol{\ell} \otimes \mathbf{c}) \mathbf{N}_{,\gamma\alpha} \quad ,\end{aligned}\tag{52}$$

where the scalars $\mathcal{L}_\alpha^\gamma$, $\mathcal{C}_\alpha^\gamma$ and $\mathcal{N}_\alpha^\gamma$ are defined as

$$\begin{aligned}\mathcal{L}_\alpha^\gamma &:= -\ell^\gamma (\lambda^{-1} c_\beta L_{,\alpha}^\beta + \ell^\beta \Gamma_{\beta\alpha}^c) \quad , \\ \mathcal{C}_\alpha^\gamma &:= \lambda^{-1} L_{,\alpha}^\gamma - \ell^\gamma (\lambda^{-1} \ell_\beta L_{,\alpha}^\beta + \ell^\beta \Gamma_{\beta\alpha}^\ell) \quad , \\ \mathcal{N}_\alpha^\gamma &:= c^\gamma \ell^\beta b_{\beta\alpha} \quad .\end{aligned}\tag{53}$$

Inserting (51) into (40) gives

$$\begin{aligned}\delta a_{\alpha\beta} &= \delta \mathbf{x}_e^\top (\mathbf{N}_{e,\alpha}^\top \mathbf{N}_{e,\beta} + \mathbf{N}_{e,\beta}^\top \mathbf{N}_{e,\alpha}) \mathbf{x}_e \quad , \\ \delta b_{\alpha\beta} &= \delta \mathbf{x}_e^\top \mathbf{N}_{e;\alpha\beta}^\top \mathbf{n} \quad , \\ \bar{M}_0^{\alpha\beta} \delta \bar{b}_{\alpha\beta} &= \delta \mathbf{x}_e^\top \mathbf{C}_{e;\alpha\beta}^{\gamma\top} \mathbf{a}_\gamma \bar{M}_0^{\alpha\beta} \quad ,\end{aligned}\tag{54}$$

where⁵

$$\mathbf{C}_{e;\alpha\beta}^\gamma := -c_{;\beta}^\gamma \mathbf{N}_{e,\alpha} - \delta_\alpha^\gamma \mathbf{C}_{e,\beta} \quad .\tag{55}$$

3.3 FE force vectors

The internal FE force vectors are obtained by inserting Eqs. (51) and (54) into Eq. (46.2). This gives

$$\mathbf{G}_{\text{int}}^e = \delta \mathbf{x}_e^\top (\mathbf{f}_{\text{int}\tau}^e + \mathbf{f}_{\text{int}M}^e + \mathbf{f}_{\text{int}\bar{M}}^e) \quad ,\tag{56}$$

where

$$\begin{aligned}\mathbf{f}_{\text{int}\tau}^e &:= \int_{\Omega_0^e} \tau^{\alpha\beta} \mathbf{N}_{e,\alpha}^\top \mathbf{a}_\beta \, dA \quad , \\ \mathbf{f}_{\text{int}M}^e &:= \int_{\Omega_0^e} M_0^{\alpha\beta} \mathbf{N}_{e;\alpha\beta}^\top \mathbf{n} \, dA \quad , \\ \mathbf{f}_{\text{int}\bar{M}}^e &:= \int_{\Omega_0^e} \bar{M}_0^{\alpha\beta} \mathbf{C}_{e;\alpha\beta}^{\gamma\top} \mathbf{a}_\gamma \, dA\end{aligned}\tag{57}$$

⁵Eq. (54.3) here is equivalent to expression (53.3) in Duong et al. (2022) but offers conciseness thanks to the definition of $\mathbf{C}_{e;\alpha\beta}^\gamma$.

denote the internal FE force vectors associated with membrane stretching, out-of-plane bending, and in-plane bending, respectively. Similarly, discretization of the external virtual work in Eq. (46.3) gives

$$G_{\text{ext}}^e = \delta \mathbf{x}_e^T (\mathbf{f}_{\text{ext}0}^e + \mathbf{f}_{\text{ext}p}^e + \mathbf{f}_{\text{ext}t}^e + \mathbf{f}_{\text{ext}m}^e + \mathbf{f}_{\text{ext}\bar{m}}^e) + \delta \mathbf{x}_A \cdot \mathbf{f}_{\text{ext}m_\nu}^A, \quad (58)$$

with the external FE forces

$$\begin{aligned} \mathbf{f}_{\text{ext}0}^e &:= \int_{\Omega_0^e} \mathbf{N}_e^T \mathbf{f}_0 \, dA, \\ \mathbf{f}_{\text{ext}p}^e &:= \int_{\Omega^e} \mathbf{N}_e^T p \mathbf{n} \, da, \\ \mathbf{f}_{\text{ext}t}^e &:= \int_{\partial_t \Omega^e} \mathbf{N}_e^T \mathbf{t} \, ds, \\ \mathbf{f}_{\text{ext}m_\tau}^e &:= - \int_{\partial_{m_\tau} \Omega^e} \mathbf{N}_{e,\alpha}^T \nu^\alpha m_\tau \mathbf{n} \, ds, \\ \mathbf{f}_{\text{ext}\bar{m}}^e &:= \int_{\partial_{\bar{m}} \Omega^e} \mathbf{N}_{e,\alpha}^T \ell^\alpha \bar{m} \mathbf{c} \, ds, \\ \mathbf{f}_{\text{ext}m_\nu}^A &:= m_\nu \mathbf{n}_A. \end{aligned} \quad (59)$$

Here, the external body force \mathbf{f} is assumed to consist of a dead load \mathbf{f}_0 and an external surface pressure p , as $\mathbf{f} = \mathbf{f}_0/J + p \mathbf{n}$.

Remark 3.1: The consistent tangent matrices resulting from the linearization of the virtual work can be found in the literature. For example, the tangents of the forces in (57) and (59) can be found in Duong et al. (2022) – see c.f. Eq. (60-64) and cf. Eq. (87) therein, respectively. Pressure loads, such as hydrostatic pressure, are discussed in Sauer et al. (2014), while Duong et al. (2024) discuss external corner forces.

4 Constitutive equations

Given the work-conjugation pairs appearing in Eq. (46), and by using the classical procedure of Coleman and Noll (1964) for hyperelasticity, the stresses and stress couples in Kirchhoff-Love shells can be obtained from the derivative of a stored energy function per reference area, denoted by W , with respect to the corresponding work-conjugate kinematic variables (Duong et al., 2023). I.e.

$$\tau^{\alpha\beta} = 2 \frac{\partial W}{\partial a_{\alpha\beta}}, \quad M_0^{\alpha\beta} = \frac{\partial W}{\partial b_{\alpha\beta}}, \quad \bar{M}_{0i}^{\alpha\beta} = \frac{\partial W}{\partial \bar{b}_{\alpha\beta}^i}. \quad (60)$$

In the presence of material anisotropy and angle elastoplasticity as considered in this work, W takes the form

$$W = W(a_{\alpha\beta}, b_{\alpha\beta}, \bar{b}_{\alpha\beta}^i; L_i^{\alpha\beta}, \phi_p), \quad (61)$$

while the constitutive relations (60) remains unchanged, see Sauer et al. (2019); Duong et al. (2023) and Remark 4.1. Here, ϕ_p is chosen as the internal variable to describe the plastic angle change between two fiber families i and j . Alternatively to Eq. (61), W can also be expressed in terms of invariants thanks to the representation theorem (Rivlin and Rideal, 1949). This is considered in the following.

A simple form of a generalized hyperelastic shell model for two-fiber-family dry fabrics is given by (Duong et al., 2023)

$$W = W_{\text{fib-stretch}} + W_{\text{fib-bending}} + W_{\text{fib-torsion}} + W_{\text{fib-angle}} , \quad (62)$$

which consists of the strain energies for fiber stretching, out-of-plane and in-plane fiber bending, fiber torsion, and elastic angle change between the two fiber families, respectively. For angle elastoplasticity, the last term is a function of the elastic angle ϕ_e from Eq. (34), instead of the total angle ϕ as in hyperelasticity, see Duong et al. (2023). A simple quadratic form for $W_{\text{fib-angle}}$ is

$$W_{\text{fib-angle}} = \frac{1}{2} \mu_f \phi_e^2 , \quad (63)$$

where material parameter μ_f can be identified as the shear modulus of fabrics, see Remark 5.1.

The other terms in Eq. (62) are taken as in the hyperelastic textile model of Duong et al. (2023),

$$\begin{aligned} W_{\text{fib-stretch}} &= \frac{1}{2} \epsilon_L \sum_{i=1}^2 (\lambda_i - 1)^2 , \\ W_{\text{fib-bending}} &= \frac{1}{2} \sum_{i=1}^2 \left[\beta_n (K_n^i)^2 + \beta_g (K_g^i)^2 \right] , \\ W_{\text{fib-torsion}} &= \frac{1}{2} \beta_\tau \sum_{i=1}^2 (T_g^i)^2 , \end{aligned} \quad (64)$$

where T_g , K_n , and K_g are defined in Eq. (24). Quantities ϵ_\bullet and β_\bullet are material parameters.

From Eq. (64) and (60), the effective stress and moment components follow as

$$\begin{aligned} \tau^{\alpha\beta} &= \epsilon_L \sum_{i=1}^2 (\lambda_i - 1) \frac{1}{\lambda_i} L_i^{\alpha\beta} + \tau_a^{\alpha\beta} , \\ M_0^{\alpha\beta} &= \beta_n \sum_{i=1}^2 K_n^i L_i^{\alpha\beta} + \beta_\tau \frac{1}{2} \sum_{i=1}^2 T_g^i (c_{0i}^\alpha L_i^\beta + c_{0i}^\beta L_i^\alpha) , \\ \bar{M}_0^{\alpha\beta} &:= \sum_{i=1}^2 \bar{M}_{0i}^{\alpha\beta} = \beta_g \sum_{i=1}^2 K_g^i L_i^{\alpha\beta} , \end{aligned} \quad (65)$$

where $\tau_a^{\alpha\beta} := 2 \partial W_{\text{fib-angle}} / \partial a_{\alpha\beta}$. The material tangents of (65) follow from Eq. (48) as

$$\begin{aligned} c^{\alpha\beta\gamma\delta} &= + \sum_{i=1}^{n_f} \epsilon_L^i \lambda_i^{-3} L_i^{\alpha\beta} L_i^{\gamma\delta} + c_a^{\alpha\beta\gamma\delta} \\ f^{\alpha\beta\gamma\delta} &= \sum_{i=1}^{n_f} \beta_n^i L_i^{\alpha\beta} L_i^{\gamma\delta} + \sum_{i=1}^{n_f} \beta_\tau^i (c_{0i}^\alpha L_i^\beta)^{\text{sym}} (c_{0i}^\gamma L_i^\delta)^{\text{sym}} , \\ \bar{f}^{\alpha\beta\gamma\delta} &:= \sum_{i=1}^{n_f} \bar{f}_{ii}^{\alpha\beta\gamma\delta} = \sum_{i=1}^{n_f} \beta_g^i L_i^{\alpha\beta} L_i^{\gamma\delta} , \\ d^{\alpha\beta\gamma\delta} &= e^{\alpha\beta\gamma\delta} = \bar{d}_i^{\alpha\beta\gamma\delta} = \bar{e}_i^{\alpha\beta\gamma\delta} = \bar{g}_i^{\alpha\beta\gamma\delta} = \bar{h}_i^{\alpha\beta\gamma\delta} = 0 , \end{aligned} \quad (66)$$

where $c_a^{\alpha\beta\gamma\delta} = 2 \partial \tau_a^{\alpha\beta} / \partial a_{\alpha\beta}$ denotes the material tangents associated with stress $\tau_a^{\alpha\beta}$. They will be derived in Sec. 5.

Remark 4.1: By applying the classical procedure of [Coleman and Noll \(1964\)](#) to thin shell elastoplasticity, [Sauer et al. \(2019\)](#) show that the stresses and moments are given by (cf. [Sauer et al. \(2019\)](#), Eq. (157))

$$\sigma^{\alpha\beta} = \frac{1}{J_e} \frac{\partial \hat{\Psi}}{\partial \varepsilon_{\alpha\beta}^e}, \quad M^{\alpha\beta} = \frac{1}{J_e} \frac{\partial \hat{\Psi}}{\partial \kappa_{\alpha\beta}^e}, \quad (67)$$

where $\varepsilon_{\alpha\beta}^e := (a_{\alpha\beta} - \hat{a}_{\alpha\beta})/2$ and $\kappa_{\alpha\beta}^e := b_{\alpha\beta} - \hat{b}_{\alpha\beta}$ are the elastic strains, and where $\hat{\Psi}$ is the Helmholtz free energy per unit intermediate configuration area. The energy per reference area then follows as $W = J_p \hat{\Psi}$. Since

$$\frac{\partial W}{\partial \varepsilon_{\alpha\beta}^e} = 2 \frac{\partial W}{\partial a_{\alpha\beta}}, \quad \frac{\partial J_p}{\partial \varepsilon_{\alpha\beta}^e} = 0, \quad \frac{\partial W}{\partial \kappa_{\alpha\beta}^e} = \frac{\partial W}{\partial b_{\alpha\beta}}, \quad (68)$$

(cf. Eqs. (78.1), (80.1), (90.1) in [Sauer et al. \(2019\)](#)), this leads to the nominal stresses $\tau^{\alpha\beta} := J \sigma^{\alpha\beta}$ and $M_0^{\alpha\beta} := J M^{\alpha\beta}$ as given in Eq. (60) above. Working with $\hat{\Psi}$ offers advantages when adapting existing hyperelasticity models to inelastic materials, as the functional form $\hat{\Psi} = \hat{\Psi}(\varepsilon_{\alpha\beta}^e, \kappa_{\alpha\beta}^e)$ (as well as stresses and material tangents) can be picked the same as that of the purely elastic case $W = W(\varepsilon_{\alpha\beta}, \kappa_{\alpha\beta})$. See [Vu-Bac et al. \(2019\)](#) for an application to thermoelastic shells.

5 Angle elastoplasticity of textiles

This section derives the stress response due to elastoplastic angle change. It follows from a given stored energy function $W_{\text{fib-angle}}(\phi_e)$, which for example is given by Eq. (63). According to Eq. (60.1) this stress is

$$\tau_a^{\alpha\beta} = 2 \frac{\partial W_{\text{fib-angle}}}{\partial a_{\alpha\beta}}. \quad (69)$$

As seen from Eqs. (36), (34) and (41), angle measure ϕ_e can be expressed in terms of the metric $a_{\alpha\beta}$. Therefore Eq. (69) can be rewritten as

$$\tau_a^{\alpha\beta} = 2 \tau \frac{\partial \phi_e}{\partial a_{\alpha\beta}}, \quad (70)$$

where we have defined the (scalar) shear stress between fiber families

$$\tau := \frac{\partial W}{\partial \phi_e}, \quad (71)$$

and where $\partial \phi_e / \partial a_{\alpha\beta}$ is determined below, see Remark 5.3. In case of model (63), τ takes the simple expression

$$\tau = \mu_f \phi_e. \quad (72)$$

The computation of ϕ_e requires the knowledge of ϕ and ϕ_p according to Eq. (36). While ϕ is observable from the current configuration (using Eq. (33)), the internal variable ϕ_p requires resorting to the intermediate configuration $\hat{\mathcal{S}}$. This is discussed in the following subsection.

Remark 5.1: For an initial fiber angle of 90 degrees and small angle changes, the quantity ϕ is equal to two times the shear strain component ε_{12} , i.e. $\phi = \theta_{12} = 2\varepsilon_{12}$. In linear elasticity, the shear stress then is $\sigma_{12} = 2\mu\varepsilon_{12}$, where μ is the shear modulus. In other words, in this case stress τ defined in Eq. (72) is the classical shear stress, while μ_f is the classical shear modulus of fabrics.

5.1 Proposed yield function and flow rule

We assume the evolution of the internal variable ϕ_p is governed by a yield function with an associated flow rule and evolution equations of independent hardening/softening variables.

The yield function for angle plasticity that includes both kinematic and isotropic hardening can be generally written in the form

$$f_y(\tau, q, p) = |\tau - f_{\text{kin}}(p)| - f_{\text{iso}}(q) , \quad (73)$$

where $f_{\text{kin}}(p)$ and $f_{\text{iso}}(q) \geq 0$ model kinematic and isotropic hardening, respectively. Here, p and q denote the corresponding hardening variables. The yield function takes the following values

$$f_y \begin{cases} < 0 & \text{elastic} , \\ = 0 & \text{plastic} . \end{cases} \quad (74)$$

In particular for textile materials, we assume there is no kinematic hardening (i.e. $f_{\text{kin}}(p) = 0$), while the isotropic hardening is governed by the scalar-valued function

$$f_{\text{iso}}(q) = \tau_y + A \operatorname{asinh}(a q) + B \tanh(b q) + C q^c , \quad (75)$$

where τ_y is the initial yield stress, while A, B, C , and a, b and c are model parameters. With Eq. (75), Eq. (73) becomes

$$f_y(\tau, q) = h \tau - \tau_y - A \operatorname{asinh}(a q) - B \tanh(b q) - C q^c , \quad \text{with } h := \operatorname{sign}(\tau) . \quad (76)$$

We further assume the associated flow rule

$$\dot{\phi}_p = \dot{\lambda} \frac{\partial f_y}{\partial \tau} , \quad (77)$$

where λ denotes the accumulated plastic angle change. Inserting (75) into Eq. (77) gives

$$\dot{\phi}_p = h \dot{\lambda} . \quad (78)$$

For the hardening variable q , we assume the simple evolution law

$$\dot{q} = \dot{\lambda} . \quad (79)$$

Remark 5.2: Choice (75) is motivated by the experimental observations in the picture frame test from [Cao et al. \(2008\)](#) shown in Fig. 8. Accordingly, we assume there are two main mechanisms governing the shear response of woven fabrics:

The first is elastoplastic angle change due to rotational friction between warp and weft yarns, which includes initial sticking and rotational sliding friction. The second is elastoplastic angle change due to yarn-yarn locking ([Cao et al., 2008](#)), where warp and weft yarns exert in-plane pressure on each other, constraining further relative rotations between them. During deformation, one mechanism dominates over the other, resulting in the three phases usually seen in the shear force versus shear angle γ curve. E.g. for the curves in Fig. 8 in particular, sticking and rotational sliding friction dominate phase I (at $\gamma < 2^\circ$, approximately) and phase II ($\gamma = 2\text{-}35^\circ$), respectively. Meanwhile yarn-yarn locking begins at around $\gamma = 35\text{-}45^\circ$ and becomes dominant at larger shear angle γ (phase III).

To reproduce such behavior, parameter τ_y in Eq. (75) sets the initial sticking limit of phase I, while the four parameters A, a, B and b reflect the low plastic resistance of phase II, and the two parameters C and c capture the increased hardening of phase III by a power law.

5.2 Time discretization and predictor-corrector algorithm

A time integration scheme is required for solving Eq. (78) and (79). Here, we employ the backward Euler scheme for both variables ϕ_p and q , i.e.

$$\begin{aligned} \phi_p^{n+1} &= \phi_p^n + h^{n+1} \Delta \lambda^{n+1} , \\ q^{n+1} &= q^n + \Delta \lambda^{n+1} . \end{aligned} \quad (80)$$

With this, the evaluation of Eq. (76) is based on a classical predictor-corrector algorithm:⁶

1. The *trial step* is to determine whether the material point is in an elastic or plastic state by assuming the former, i.e. setting the increment of the plastic strain to $\Delta\lambda = 0$. This gives the current elastic trial angle

$$\phi_e^{\text{trial}} = \phi^{n+1} - \phi_p^n \quad (81)$$

due to Eq. (80.1) and Eq. (36). Thus the current trial stress (72) becomes

$$\tau^{\text{trial}} := \mu_f \phi_e^{\text{trial}} . \quad (82)$$

The verification of the elastic assumption is then based on the value of the yield function (76) computed in this step,

$$\begin{aligned} f_y^{\text{trial}} &:= h^{\text{trial}} \tau^{\text{trial}} - \tau_y - A \operatorname{asinh}(a q^n) - B \tanh(b q^n) - C (q^n)^c , \\ h^{\text{trial}} &:= \operatorname{sign}(\tau^{\text{trial}}) . \end{aligned} \quad (83)$$

2. If $f_y^{\text{trial}} \leq 0$, then the material is indeed in an *elastic state*. Thus

$$\begin{aligned} \tau &= \tau^{\text{trial}} , \\ \phi_e &= \phi_e^{\text{trial}} . \end{aligned} \quad (84)$$

Taking the variation of the last equation in (84) and considering Eq. (81) and (41), gives

$$\delta\phi_e = \delta\theta_{12}^{n+1} = g_{12}^{\alpha\beta} \delta a_{\alpha\beta} , \quad (85)$$

such that Eq. (69) leads to the stress components

$$\tau_a^{\alpha\beta} = 2 \tau^{\text{trial}} g_{12}^{\alpha\beta} . \quad (86)$$

The corresponding material tangents follows from Eq. (48) as

$$c_a^{\alpha\beta\gamma\delta} = 4 \epsilon g_{12}^{\alpha\beta} g_{12}^{\gamma\delta} + 4 \tau^{\text{trial}} g_{12}^{\alpha\beta\gamma\delta} , \quad (87)$$

where $g_{12}^{\alpha\beta}$ and $g_{12}^{\alpha\beta\gamma\delta}$ are defined by Eq. (42) and (44), respectively.

3. If $f_y^{\text{trial}} > 0$, then the state is plastic. An evaluation of plastic strain $\Delta\lambda > 0$ is then required for the correction of the trial state. The computation of plastic strain $\Delta\lambda$ is found such that Eq. (76) satisfies

$$f_y^{n+1} = h^{n+1} \tau^{n+1} - \tau_y - A \operatorname{asinh}(a q^{n+1}) - B \tanh(b q^{n+1}) - C (q^{n+1})^c = 0 , \quad (88)$$

where τ^{n+1} is now computed from

$$\tau^{n+1} = \mu_f (\phi^{n+1} - \phi_p^{n+1}) . \quad (89)$$

By considering Eq. (80.1), (82) and (81), Eq. (89) becomes

$$\tau^{n+1} = \tau^{\text{trial}} - h^{n+1} \mu_f \Delta\lambda . \quad (90)$$

⁶Henceforth, unless indicated otherwise, variables without time step superscript are evaluated at the current time step $n + 1$.

Given that parameters $\mu_f > 0$ and $\Delta\lambda > 0$, Eq. (90) leads to

$$h^{n+1} = h^{\text{trial}} . \quad (91)$$

Inserting Eq. (91), (90) and (80.2) into (88) gives

$$\begin{aligned} g(\Delta\lambda) &:= h^{\text{trial}} \tau^{\text{trial}} - \mu_f \Delta\lambda - \tau_y \\ &- A \operatorname{asinh}[a(q^n + \Delta\lambda)] - B \tanh[b(q^n + \Delta\lambda)] - C (q^n + \Delta\lambda)^c = 0 , \end{aligned} \quad (92)$$

which is solved for $\Delta\lambda$ using Newton's method. For this, the derivative

$$g' = -\mu_f - \frac{A a}{\sqrt{1 + a^2 (q^n + \Delta\lambda)^2}} - B b \operatorname{sech}^2[b(q^n + \Delta\lambda)] - C c (q^n + \Delta\lambda)^{c-1} \quad (93)$$

is needed. With $\Delta\lambda$ evaluated, the elastic angle strain and stress can then be updated from

$$\begin{aligned} \phi_p^{n+1} &= \phi_p^n + h^{\text{trial}} \Delta\lambda , \\ \phi_e^{n+1} &= \phi^{n+1} - \phi_p^{n+1} , \\ q^{n+1} &= q^n + \Delta\lambda , \\ \tau^{n+1} &= \mu_f \phi_e^{n+1} . \end{aligned} \quad (94)$$

From Eq. (94.2) follows the elastic angle variation

$$\delta\phi_e = \delta\phi_e^{n+1} = \delta\phi^{n+1} = \delta\theta_{12}^{n+1} = g_{12}^{\alpha\beta} \delta a_{\alpha\beta} , \quad (95)$$

the stress components (69)

$$\tau_a^{\alpha\beta} = 2\tau g_{12}^{\alpha\beta} , \quad (96)$$

and the corresponding material tangent (48)

$$c_a^{\alpha\beta\gamma\delta} = 4(\mu_f + \mu_f^2/g') g_{12}^{\alpha\beta} g_{12}^{\gamma\delta} + 4\tau g_{12}^{\alpha\beta\gamma\delta} . \quad (97)$$

The resulting predictor-corrector algorithm is summarized in Tab. 1.

Remark 5.3: As seen from Eq. (85) and (95), the change of elastic angle ϕ_e with respect to the metric in the presented plasticity model is simply

$$\frac{\partial\phi_e}{\partial a_{\alpha\beta}} = g_{12}^{\alpha\beta} \quad (98)$$

for both elastic and plastic states.

6 Picture frame test

This section first verifies the preceding finite element formulation using the analytical solution of the proposed angle plasticity model for the picture frame test given in Appendix B. Second, the picture frame test is used to investigate the influence of the model parameters. In these results, shear forces are normalized by frame length L_0 and a reference stress μ_0 .

Given: current fiber angle ϕ^{n+1} , the previous values ϕ^n , ϕ_p^n , q^n , shear stiffness μ_f , and yield function f_y .

1. Trial step with the elastic assumption: $\phi_e^{\text{trial}} = \phi^{n+1} - \phi_p^n$, and $\tau^{\text{trial}} = \epsilon \phi_e^{\text{trial}}$
 - Compute trial yield function $f_y^{\text{trial}} := f_y(\tau^{\text{trial}}, q^n)$ from Eq. (83).
2. If $f_y^{\text{trial}} \leq 0$, then the step is indeed elastic.
 - Set plastic strain $\Delta\lambda = 0$.
 - Compute elastic angle strain ϕ_e^{n+1} and elastic shear stress τ from Eq. (84).
 - Compute stress $\tau_a^{\alpha\beta}$ and corresponding tangents $c_a^{\alpha\beta\gamma\delta}$ from Eq. (86) and (87).
4. If $f_y^{\text{trial}} > 0$, then the step is plastic:
 - Compute plastic strain $\Delta\lambda$ using Newton's method with residual (92) and gradient (93).
 - Compute elastic angle strain ϕ_e^{n+1} and elastic shear stress τ from Eq. (94).
 - Compute stress $\tau_a^{\alpha\beta}$ and corresponding tangents $c_a^{\alpha\beta\gamma\delta}$ from Eq. (96) and (97).
5. Update ϕ_p and q from Eq. (80)

Table 1: Summary of the predictor-corrector algorithm.

6.1 Model verification using the picture frame test

The picture frame test consists of a square sheet of dimension $L_0 \times L_0$ with two embedded fiber families that is deformed into a rhombus as seen Fig. 3a-b. The deformation is applied by the Dirichlet boundary condition

$$\bar{\mathbf{x}}(\varphi, \bar{\mathbf{X}}) = \sqrt{2} (\cos \varphi \mathbf{e}_1 \otimes \mathbf{e}_1 + \sin \varphi \mathbf{e}_2 \otimes \mathbf{e}_2) \bar{\mathbf{X}}. \quad (99)$$

Here, $\varphi := (\pi - \theta)/2$, and $\bar{\mathbf{x}}$ and $\bar{\mathbf{X}}$ denote the current and initial position of the boundary points, respectively. The plasticity model from Sec. 4 is used in the test. Assuming no wrinkling occurs, the problem can be solved analytically, as is shown in Appendix B. Fig. 3c shows that the finite element solution and analytical solution of the shear forces are identical (within machine precision). This verifies the implemented finite element formulation.

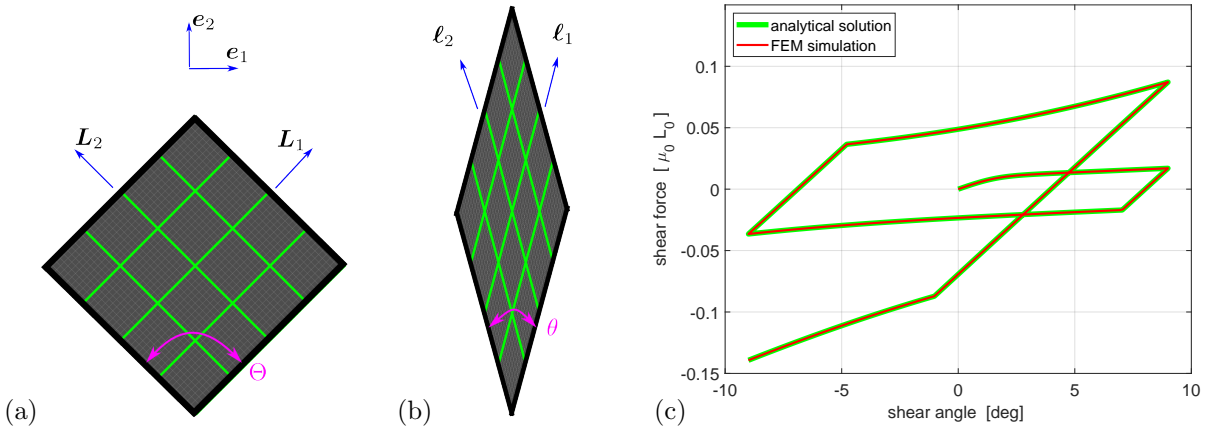


Figure 3: Verification of the proposed angle plasticity model using the picture frame test: (a) Initial and (b) deformed configurations with two fiber families (marked in green). (c) Comparison of FEM results with analytical solution for multiple loading and unloading cycles. Here, the following parameters are used: $\tau_y = 0$, $\mu_f = \mu_0$, $A = 0.05 \mu_0$, $a = 1$, $B = 0.01 \mu_0$, $b = 55$, $C = 0.7 \mu_0$ and $c = 5$.

6.2 Parameter study based on the picture frame test

In the following, the picture frame test is used to study the influence of the parameters appearing in the angle plasticity model (75) on the shear response. Additionally, the agreement between simulation and exact solution is confirmed in all cases.

6.2.1 Influence of tensile stiffness, initial shear modulus and yield stress

Tensile fiber stiffness ϵ_L has no influence on the shear response of fabrics when it is sufficiently large. Fig. 4a-b shows the influence of yield stress τ_y and initial shear modulus μ_f on to the elastic shear response of fabrics (phase I, see Remark. 5.2). As expected, parameter τ_y offsets the curve vertically, while μ_f controls its slope within the elastic range.

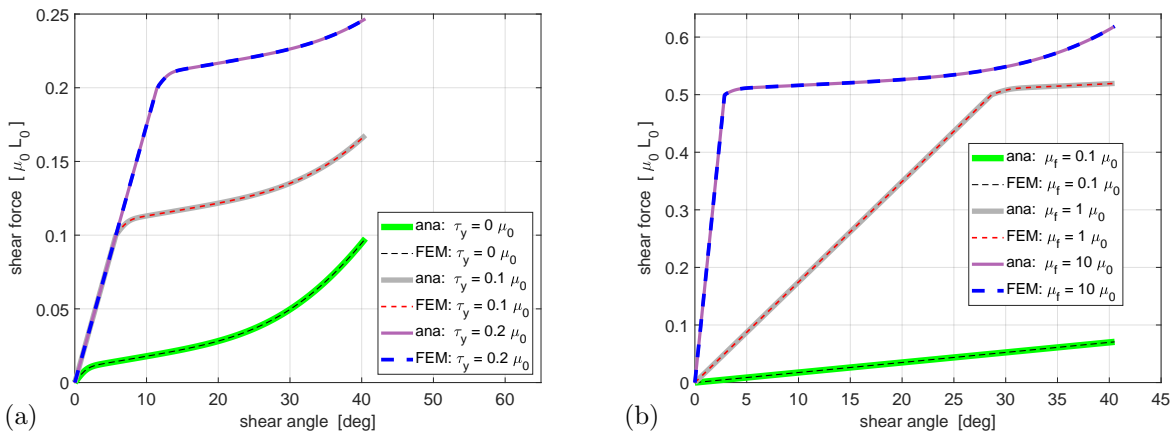


Figure 4: Parameter study based on the picture frame test during phase I: influence of (a) yield stress τ_y and (b) initial shear modulus μ_f of model (76). Here, unless otherwise varied and specified in the figure legends, the following parameters are used: $\tau_y = 0.5 \mu_0$, $\mu_f = \mu_0$, $A = 0.05 \mu_0$, $a = 1$, $B = 0.01 \mu_0$, $b = 55$, $C = 0.7 \mu_0$ and $c = 5$.

6.2.2 Influence of angle plasticity parameters

Fig. 5a-d show the influence of parameters A , a , B , and b in the proposed plasticity model (75). This set of parameters govern the low plastic resistance phase (phase II, see Remark. 5.2). Note that τ_y is set to zero here, so that no elasticity is present. Parameters A and a change the global slope and offset of the curve as seen in Fig. 5a-b, while parameters B and b control the slope and offset at small shear angles as shown in Fig. 5c-d.

On the other hand, parameters C and c govern the shear response during phase III (see Remark. 5.2) in the fabric. They thus only alter the later part of the curve as seen in Fig. 6. In theory, $\gamma = 90^\circ$ is the limit of deformation as the frame area reaches zero. Although the power law with parameters C and c does not strictly prevent this limit state, the computation becomes infeasible due to a negative finite element Jacobian. In practice, due to a finite yarn thickness, the shear force usually changes rapidly for shear angles that are far from this limit state. For example, the data in Fig. 8 shows that phase III already begins around $\gamma = 35-45^\circ$.

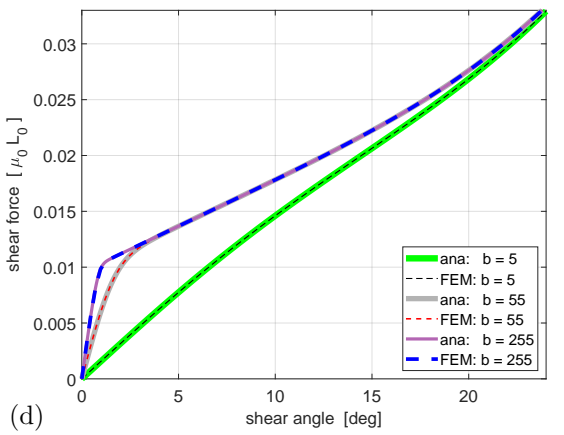
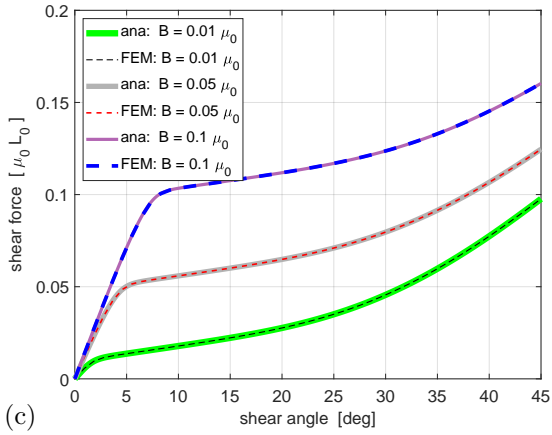
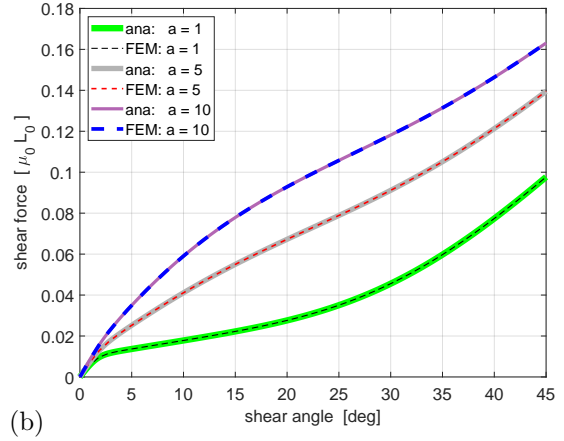
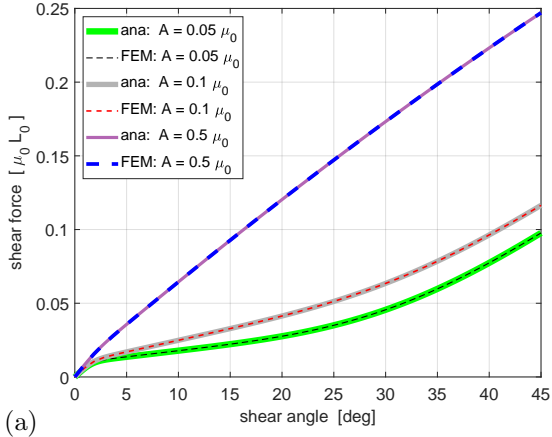


Figure 5: Parameter study based on the picture frame test during the phase II: (a)-(d) influence of parameter A , a , B and b , respectively, of model (76). These parameters govern the low plastic resistance phase (phase II). Here, unless otherwise varied and specified in the figures, the following parameters are used: $\tau_y = 0$, $\mu_f = \mu_0$, $A = 0.05 \mu_0$, $a = 1$, $B = 0.01 \mu_0$, $b = 55$, $C = 0.7 \mu_0$ and $c = 5$.

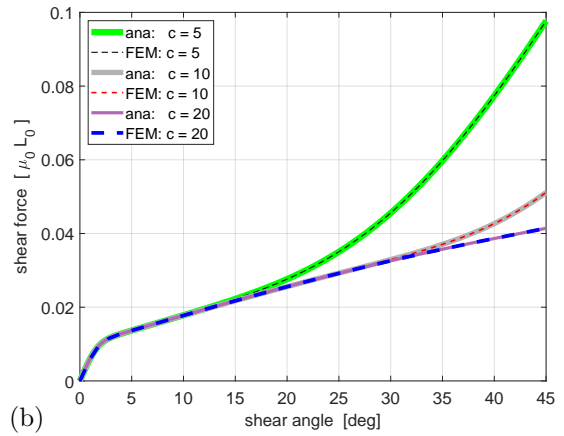
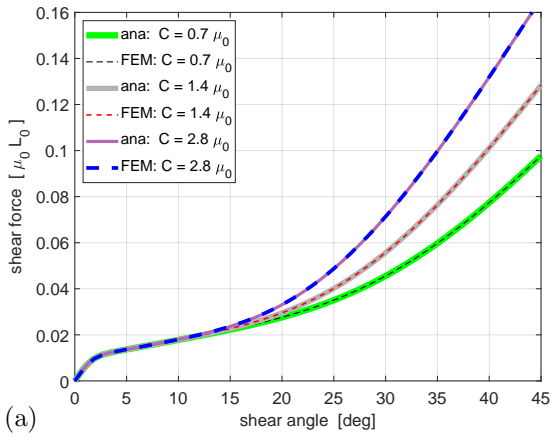


Figure 6: Parameter study based on the picture frame test during phase III: (a)-(b) influence of parameter C and c , respectively, of model (76). These parameters govern the increased hardening phase (phase III). Here, $\tau_y = 0$, $\mu_f = \mu_0$, $A = 0.05 \mu_0$, $a = 1$, $B = 0.01 \mu_0$, $b = 55$ are used.

7 Model calibration and validation

The section presents the calibration and validation of the proposed angle plasticity model. The case of plain weave (glass) fabrics is considered using experimental data provided in the literature.

7.1 Model calibration

The following three subsections discuss the calibration of all the different material parameters. The results are summarized in Tab. 2.

para.	value	unit	physical meaning	calibrated from
μ_f	5.0	N/mm	initial fabric shear modulus	pic. frame (LSMP): Cao et al. (2008)
τ_y	10^{-4}	N/mm	initial fabric yield stress	assumption
A	8.8	N/mm	yield function parameter #1	pic. frame (KUL): Cao et al. (2008)
a	0.0024	-	yield function parameter #2	pic. frame (KUL): Cao et al. (2008)
B	0.0028	N/mm	yield function parameter #3	pic. frame (KUL): Cao et al. (2008)
b	65.0	-	yield function parameter #4	pic. frame (KUL): Cao et al. (2008)
C	1.0	N/mm	yield function parameter #5	pic. frame (UN & UML): Cao et al. (2008)
c	11.0	-	yield function parameter #6	pic. frame (UN & UML): Cao et al. (2008)
ϵ_L	110.0	N/mm	tensile fabric stiffness	uniaxial tensile: Peng and Cao (2005)
β_n	3.023	N mm	out-of-plane fabric bend. stiffness	fiber cantilever: Quenzel et al. (2022)
β_g	3.023	N mm	in-plane fabric bend. stiffness	assumption
β_τ	3.023	N mm	fiber torsion stiffness	assumption

Table 2: Calibrated material parameters of fabric model (62) suitable to plane weave fabrics of glass fibers. Here, we use the following data sources reported by [Peng and Cao \(2005\)](#); [Cao et al. \(2008\)](#) and [Quenzel et al. \(2022\)](#) to fit the proposed plasticity model: Laboratoire de Mécanique des Systèmes et des Procédés (LSMP), Katholieke Universiteit Leuven in Belgium (KUL), University of Nottingham in UK (UN), and University of Massachusetts Lowell in USA (UML).

7.1.1 Calibration of the initial tensile and shear modulus of plain weave fabric

Tensile stiffness ϵ_L in Eq. (64.1) can be calibrated from experimental data of uniaxial tensile tests as shown in Fig. 7a. Here, in order to account for the undulation of yarns within the fabric, we use the tensile data provided by [Peng and Cao \(2005\)](#) for fabric samples instead of a single yarn, and our model is fitted to the data such that the initial slopes are matched.

Initial fabric shear modulus μ_f in Eq. (72), on the other hand, needs to be calibrated from a shear test, such as the picture frame test, as shown in Fig. 7b. Here, the data set from Laboratoire de Mécanique des Systèmes et des Procédés (LSMP) ([Cao et al., 2008](#)) is used, since it was obtained from the largest ratio of the fabric length (240mm, excluding the clamp-affected zone) to the frame length (245mm), cf. Tab. 3 in [Cao et al. \(2008\)](#). Such a setup maximizes the interaction between yarns in the initial loading phase, which may contribute to the largest initial slope among other testing setups as seen in Fig. 8a and Fig. 25 in [Cao et al. \(2008\)](#).

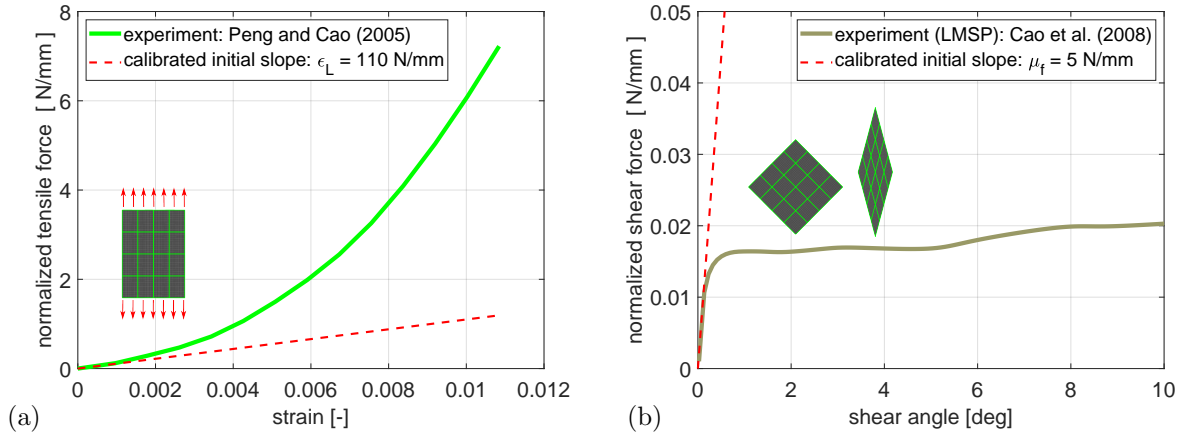


Figure 7: Model calibration of the initial tensile stiffness ϵ_L and initial elastic shear modulus μ_f for plain weave dry fabric – see Eq. (64.1) and (72), respectively – from (a) uniaxial tensile test and (b) picture frame test, respectively. The former uses the experimental data of the uniaxial tensile test averaged over the four fabric samples provided by Peng and Cao (2005). The latter uses the data for the shear force normalized by the frame length, reported by Laboratoire de Mécanique des Systèmes et des Procédés (LMSP) in Cao et al. (2008). The shear angle is defined as $\gamma := 90^\circ - \theta$.

7.1.2 Calibration of the proposed yield function

The material parameters required to calibrate the proposed yield function (76) are τ_y , A , a , B , b , C , and c – see also Remark 5.2. In principle, these seven parameters can be determined from the picture frame test. However there is no unloading data available for glass fibers in the literature. We therefore assume that the initial yield stress τ_y has a small value (10^{-4} N/mm). This is justified since rotational sliding between warp and weft yarns is expected to start for small shear angles already.

Apart from τ_y , the four parameters A , a , B , b – governing the rotational sliding between yarns – are fitted to the experimental data from Cao et al. (2008), as shown in Fig. 8a. As seen, there is large scattering between the experimental data from different sources. In particular, the LMSP data – while its first phase is useful in determining the initial shear modulus (see Sec. 7.1.1) – becomes unsuitable for the purpose of fitting A , a , B , b , since its second phase contains the shear resistance of the yarns at the sample edges due to the large fabric-frame length ratio used. The data from KUL, on the other hand, is more suitable (up to the point of the increased hardening phase) since it was obtained from three repetitions on a single sample. It was reported that, the second and the third repetitions gave similar data that was significantly lower than the first instance (KUL 1st). It is noticeable in Fig. 8a that the KUL 1st curve lies approximately at the mean of the data from UN, HKUST, and UML. This leads to our conjecture that the rotational sliding phase of the KUL 3rd curve is more accurate than the others, and we therefore use it to calibrate parameters A , a , B , b in our proposed model.

For the calibration of parameters C and c – governing the increased hardening behavior (phase III), see Remark 5.2 – the KUL data is insufficient as it does not go far enough as is seen from Fig. 8a. We therefore calibrate C and c such that the third phase of the curve from our model approximately matches the slope of the UN and UML curves. This is seen in Fig. 8a.

Further, we verify the applicability of the frame length normalization employed for our calibration by plotting the shear force versus shear angle in Fig. 8b. As seen, the curve for our fitted model is in good agreement with the KUL 3rd curve up to a shear angle of 25 degrees. After that, our proposed curve deviates from the KUL 3rd curve but it still generally follows the trend of the UN and UML curves.

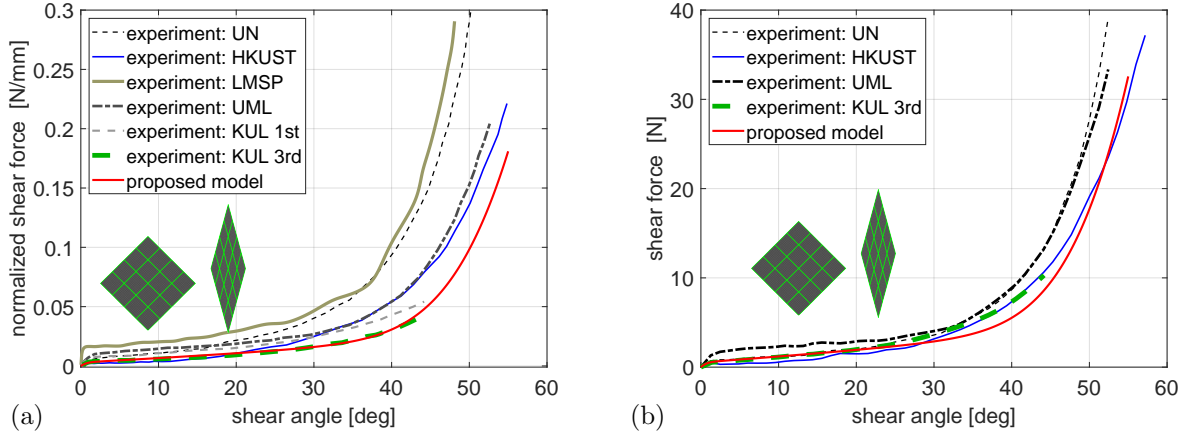


Figure 8: Model calibration for the yield function parameters A , a , B , b , C , and c – see Eq. (76) – from the picture frame test for (a) the shear force normalized by the frame length, and (b) the shear force that has been scaled by the equivalent fabric size $L_0 = 180\text{mm}$. I.e. $F_{\text{scaled}} := (L/L_0) F_{\text{reported}}$, where F_{reported} denotes the shear force reported from experiments with fabric length L . Here, the experimental curves for the normalized shear force and for F_{reported} are taken from Fig. 25 and Fig. 22, respectively, in Cao et al. (2008) for the various data sources. In the figure legend, HKUST stands for Hong Kong University of Science and Technology.

7.1.3 Calibration of other parameters

Finally, we need to calibrate the bending stiffnesses β_n and β_g and torsional stiffness β_τ for fiber bending model (64.3-4). For β_n and β_g , we use the value of 3.023 N/mm from the bending test of a single yarn reported in Quenzel et al. (2022). To the best of our knowledge, no data for the torsion of yarns is available in the literature. We thus use $\beta_\tau = 3.023\text{ N/mm}$ in our simulations.

7.2 Model validation using the bias extension test

This section validates our calibrated plasticity model using the bias extension test for a rectangular sheet of plain weave fabric (Cao et al., 2008). We consider the six samples listed in Tab. 3. These samples vary in size, but can be grouped into three sample classes based on the appearing aspect ratios 1:2, 1:2.5 and 1:3. The three sample classes are discretized by 32×64 , 32×80 and 32×96 quadratic NURBS finite elements, respectively. The calibrated material parameters from Tab. 2 are used in all subsequent computations.

sample	size [mm ²]	aspect ratio	experiment data source
#1	100 × 200	1:2	UN
#2	115 × 230	1:2	HKUST, INSA-NU
#3	150 × 300	1:2	INSA-NU
#4	100 × 250	1:2.5	UN
#5	100 × 300	1:3	UN, INSA-NU
#6	150 × 450	1:3	INSA-NU

Table 3: List of considered samples for the model verification using the bias extension test. The experimental data – here extracted from Cao et al. (2008) cf. Fig. 38 therein – originates from different institutions: University of Nottingham in UK (UN), Hong Kong University of Science and Technology (HKUST), INSA-Lyon in France and Northwestern University in USA (INSA-NU).

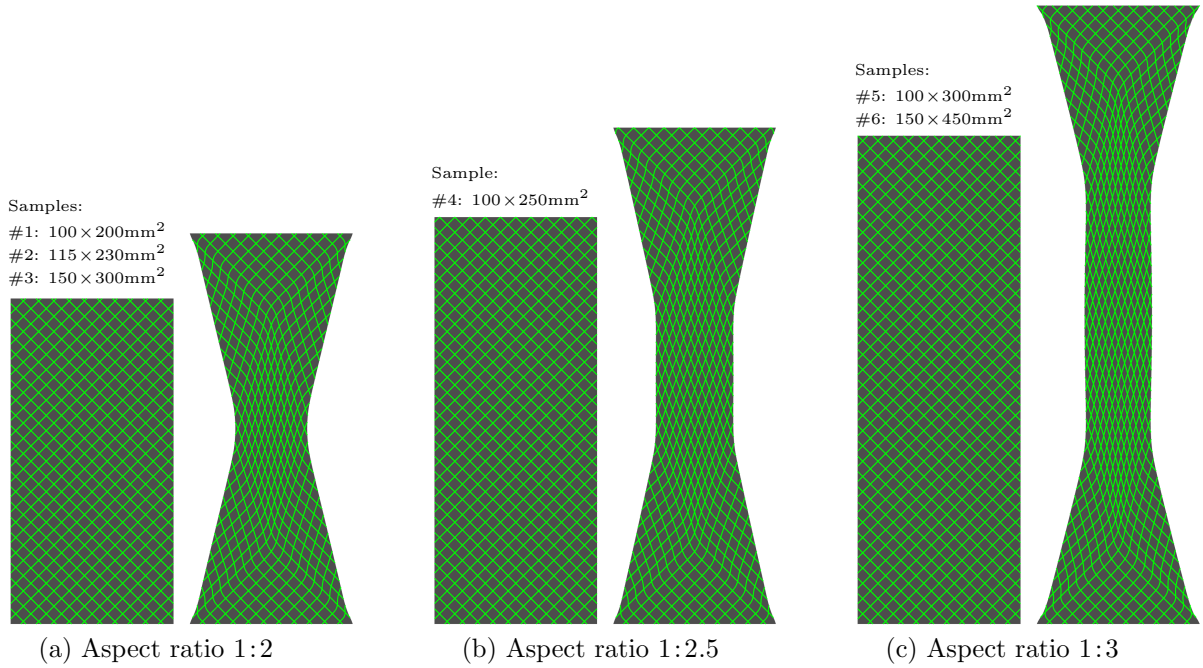


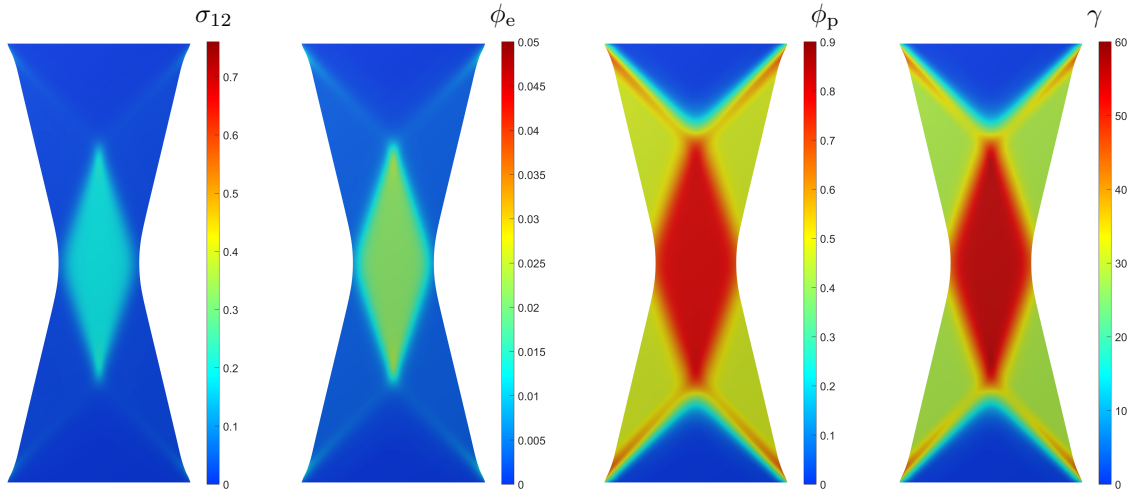
Figure 9: Bias extension test for three samples classes of plain weave fabrics: Initial and deformed configurations resulting from our computations. The deformed shapes with the same aspect ratio are almost identical regardless of size. The green lines illustrate the considered two fiber families.

Fig. 9 shows the initial and deformed configurations resulting from our simulations. Regardless of difference in size, almost identical shapes are expected for the same aspect ratio due to the relatively small bending stiffness used (see Tab. 2). This is confirmed in our computations.

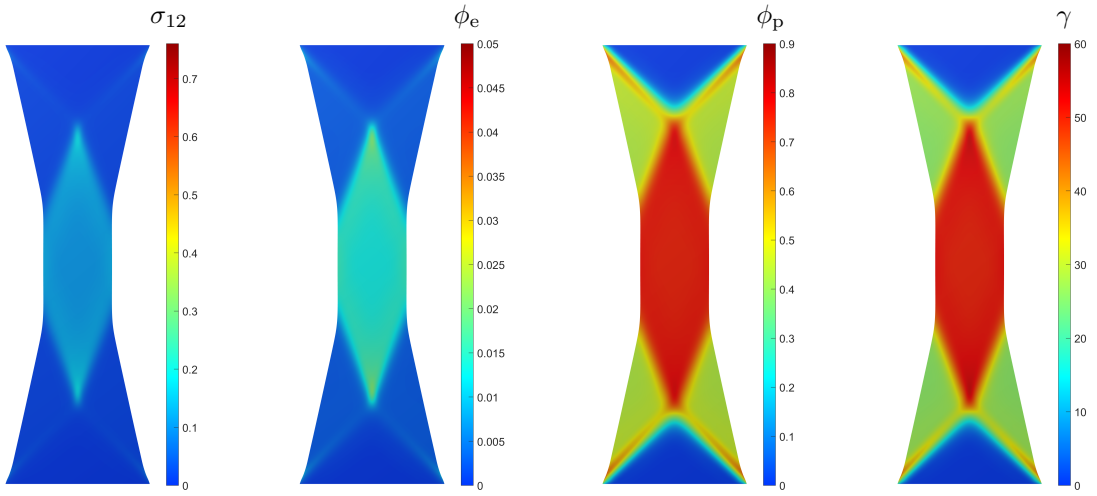
Next, Fig. 10 shows the distributions of shear stress σ_{12} , elastic angle strain ϕ_e , plastic angle strain ϕ_p and total shear angle $\gamma := 90^\circ - \arccos(\theta_{12})$ resulting from our simulations for all samples. As seen from Fig. 10 (2. & 3. column), plastic angle ϕ_p is much larger than elastic angle ϕ_e . This reflects the small yield stress τ_y and consequently leads to small ϕ_e and small stress σ_{12} . As is also seen from the plots of shear angle γ in Fig. 10 (4. column), γ is not only non-zero at the center of the samples, but also at the off-center. Note that γ is observable from experiments and our computations are consistent with the optical measurement presented in Cao et al. (2008) (cf. Fig. 37 therein – note that the shear angle was defined there by $\arccos(\theta_{12})$ in degrees). Our simulation results in Fig. 10 (1 & 2. column) further show that nonzero ϕ_e (and hence σ_{12}) mostly concentrate at the center and the shear bands of the samples. This is reasonable since the total shear angle γ is also large there – see Fig. 10 (4. column) – which corresponds to the increased hardening phase (phase III) (which already starts at around $\gamma = 35\text{-}45^\circ$, as seen from Fig. 8a.). Meanwhile γ is relatively small ($\gamma = 25^\circ$) away from the center, which still allows fibers to freely rotate against each other there.

Further, Fig. 11 compares our simulation results to the experimental results for the vertical reaction force (pulling force) versus the vertical displacement. As seen, our model generally agrees well with the experiments, especially for samples #2, #4 and #6. Since these experimental results have not been used for calibration they validate our proposed model. The results from sample #5 show that the experimental results can vary strongly for different data sources. Our results lie in-between this variation.

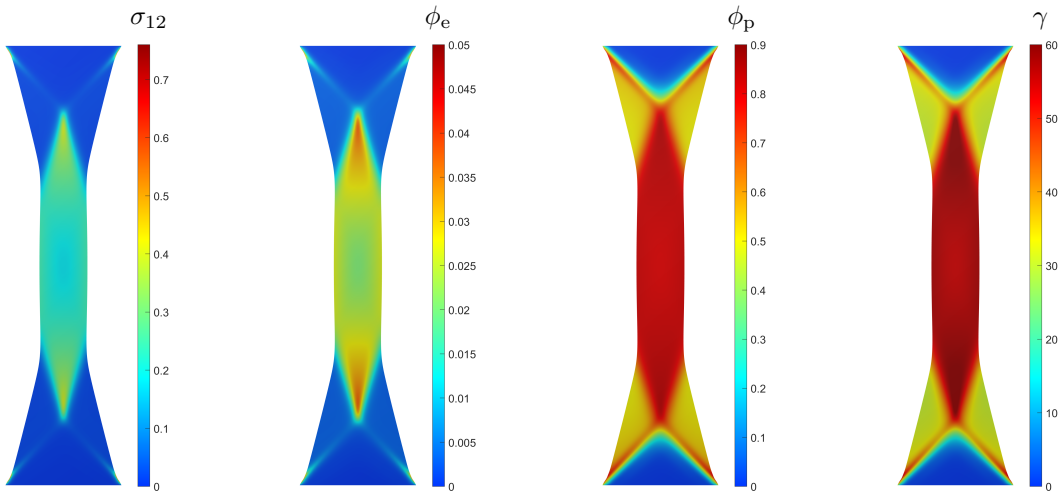
Finally, we check if the experimental data from different sources is consistent for different sample sizes. Therefore we plot the normalized reaction forces in Fig. 12. As seen, our simulation curves are almost identical for the same aspect ratio. The experimental data curves are generally consistent at low displacements, but scattered at large displacements. Our prediction lie approximately at the mean values of the experimental curves as Fig. 12 show.



(a) Aspect ratio 1:2

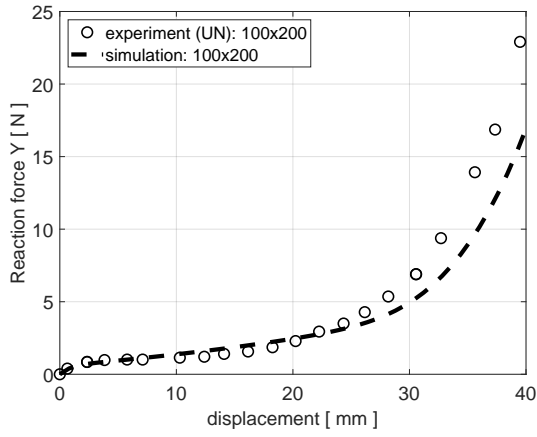


(b) Aspect ratio 1:2.5

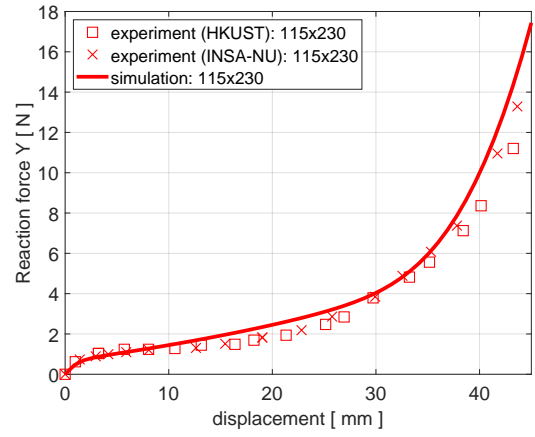


(c) Aspect ratio 1:3

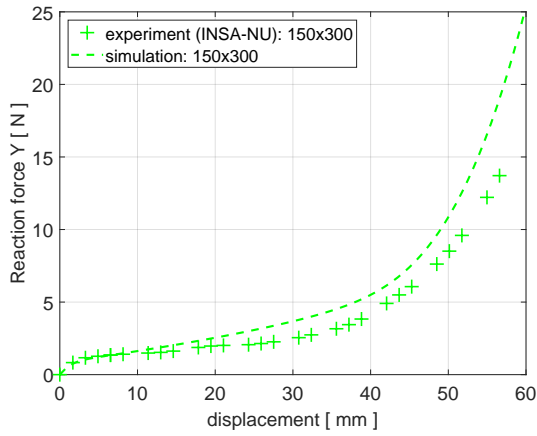
Figure 10: Bias extension test of plain weave fabrics: From left to right: True shear stress $\sigma_{12} := \tau/J$ [N/mm] according to Eq. (71), elastic angle strain ϕ_e , plastic angle strain ϕ_p , and total shear angle defined by $\gamma := 90^\circ - \arccos(\theta)$ [deg] for the three sample classes with initial aspect ratio (a) 1 : 2, (b) 1:2.5, and (c) 1:3.



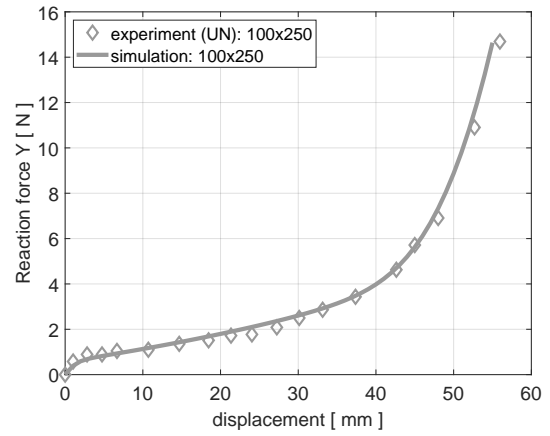
(a) sample #1



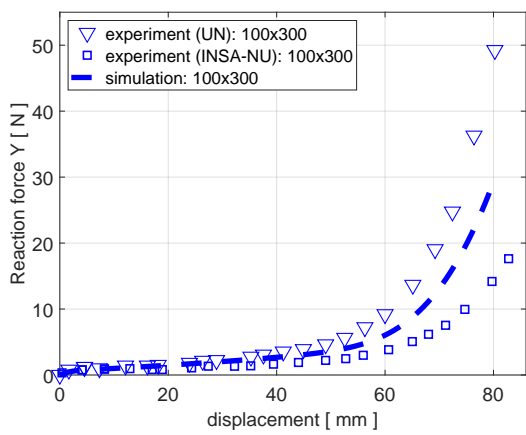
(b) sample #2



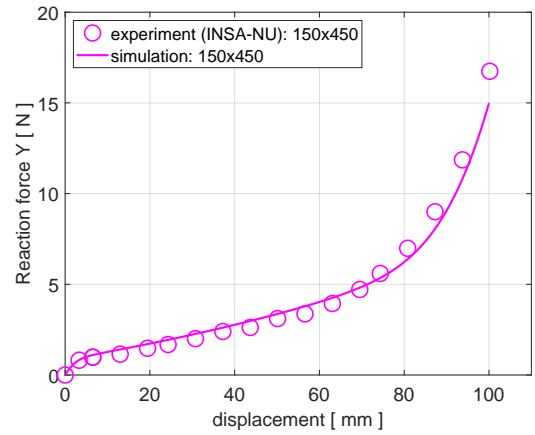
(c) sample #3



(d) sample #4

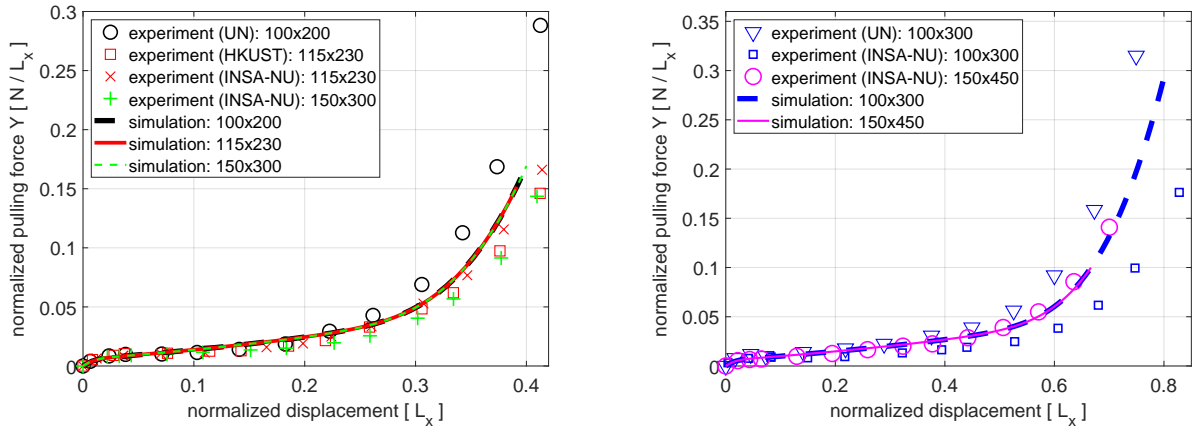


(e) sample #5



(f) sample #6

Figure 11: Bias extension test of plain weave fabrics: Comparison of results from computation and experiment for reaction force versus displacement for all the six samples. Since these experimental results have not been used for calibration they validate our proposed model.



(a) Aspect ratio 1:2

(b) Aspect ratio 1:3

Figure 12: Bias extension test of plain weave fabrics: Comparison of results from computation and experiment for normalized reaction force versus displacement for the samples with equal aspect ratios. The reaction force and the displacement are normalized by the corresponding sample widths.

8 Three-dimensional example

The last example demonstrates that the proposed angle plasticity model – which is a 2D model within the tangent plane – also works in the presence of large 3D deformations. Therefore, the following twisting example is considered: A cylindrical textile band with initial radius $R_b = 45 L_0$ and width $67.5 L_0$, see Fig. 13, is placed in contact with two rigid cylindrical tubes with radius $r_c = 9 L_0$ and distance $L_c = 72.0009 L_0$. This placement leaves a small initial penetration necessary for stabilizing contact within the penalty formulation. The textile band is discretized by 7×34 quadratic NURBS finite elements. The material parameters from Tab. 2 are used for the textile band. For the subsequent simulation, the finite element nodes on the twisting axis are fixed in the horizontal directions in order to prevent rigid body motion of the textile band.

Before twisting, the textile band is first stretched by moving the cylindrical tubes apart by $\bar{u}_z^{\max} = 4.0 r_c$ within 40 load steps. The stretched configuration has minor angle plasticity and is shown in Fig. 15 (first column). The textile band is then twisted by applying a rotation to both the upper and the lower tubes in opposite directions from starting angle $\phi \equiv 0^\circ$ up to $\phi \equiv \phi_{\max}/2$ with $\phi_{\max} = 240^\circ$. Finally, the textile band is untwisted back to starting angle $\phi \equiv 0^\circ$. The twisting and untwisting uses 2 load steps per degree. The contact force resulting from the above loading sequence is shown in Fig. 14a.

For an efficient contact simulation, we employ an adaptive penalty parameter for contact between the textile band and the cylindrical tubes as shown in Fig. 14b. Further, in order to restrict the source of dissipation to angle plasticity, sticking is assumed during textile self-contact (by using a very large friction coefficient). Thus no energy is dissipated due to textile self-contact, while at the same time this helps to stabilize the textile band at large deformations (due to an increase of the effective stiffness for in-plane shear and out-of-plane bending at the contact zone).

In order to stabilize the textile band for fiber compression, we employ here the stabilization technique proposed by [Duong et al. \(2022\)](#) with $\epsilon_{\text{stab}}^e = 10 \mu_0$, and $\epsilon_{\text{stab}}^v = 100 \mu_0$. Further, to deal with the instability due to shell buckling, we use mass-proportional (Rayleigh) damping with proportionality coefficient $\nu = 10^{-8} \mu_0 \Delta t$, where Δt denotes the (pseudo) time increment, taken as unity in the example.

Fig. 15(a-c) plot the shear stress, elastic angle ϕ_e , and plastic angle ϕ_p , respectively. As the figures show residual deformations and stresses remain after unloading. The results demonstrate that the proposed plasticity model can be also used for large 3D deformations.

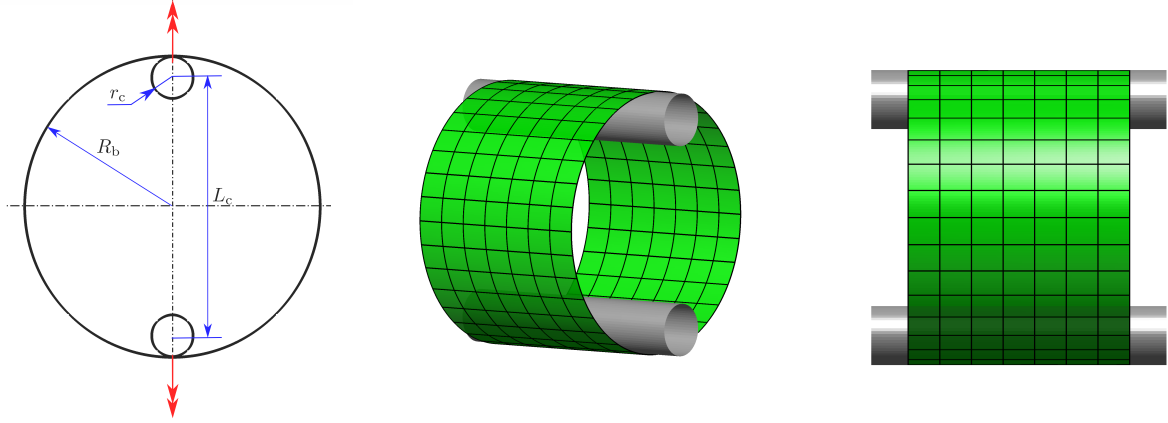


Figure 13: Stretching of a textile band: Initial configuration at different views (from left to right): Side view, 3D view, and front view, respectively.

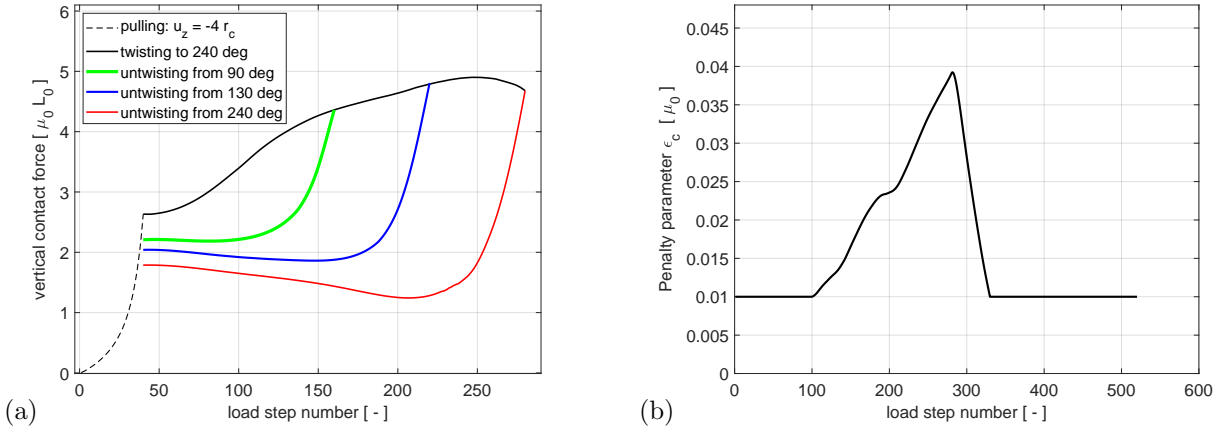
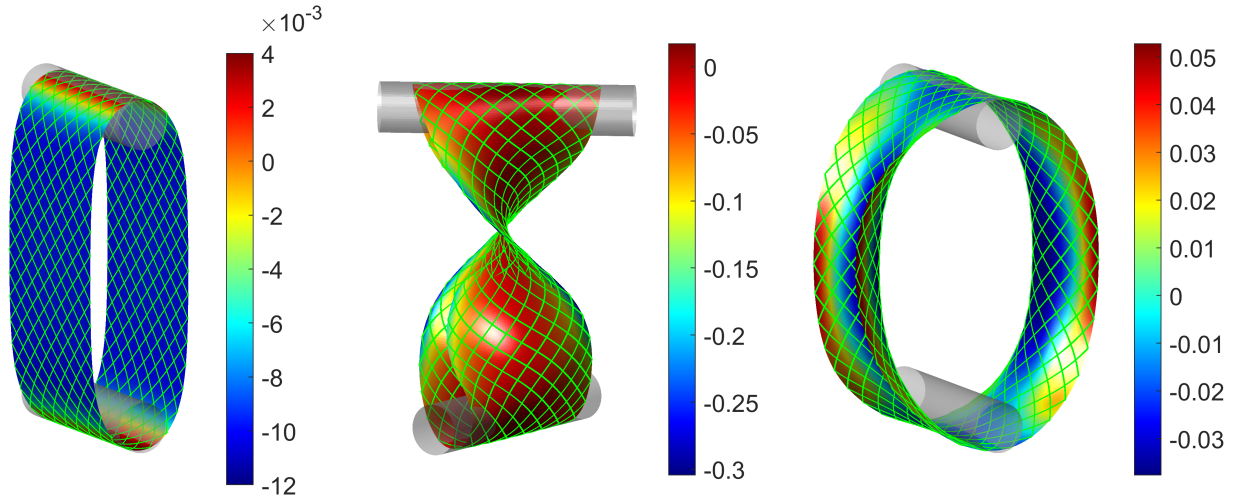
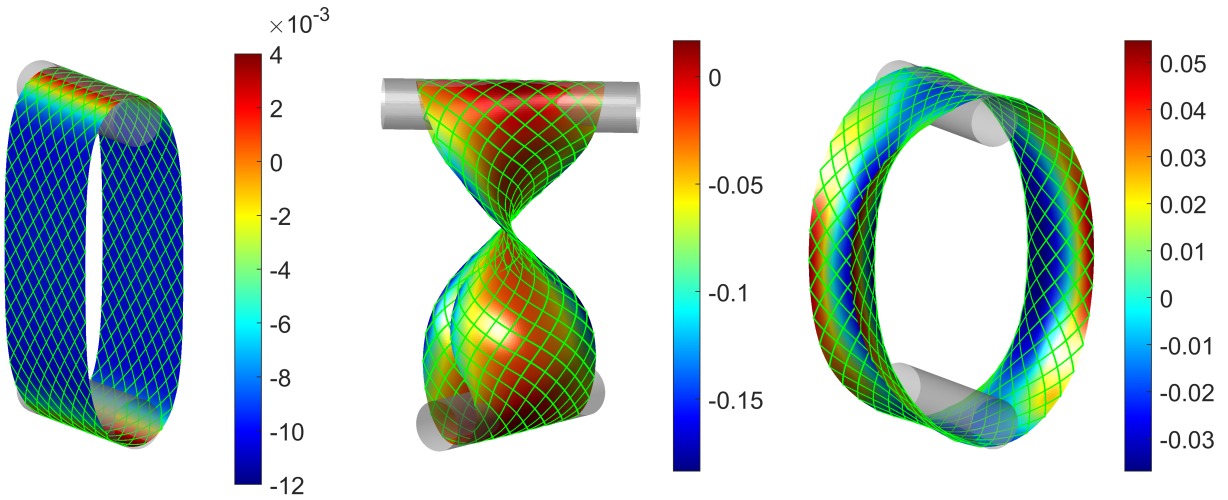


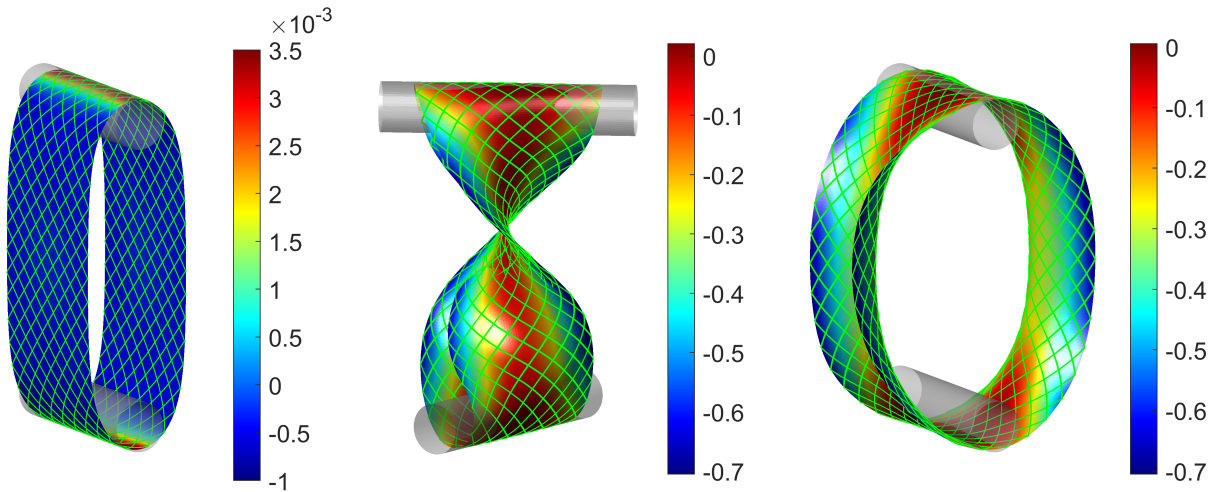
Figure 14: Twisting of a textile band: (a) vertical reaction (i.e. contact) force and (b) penalty parameter versus load step number. The load step number in (a) is reversed during unloading.



(a) shear stress σ_{12} [μ_0]



(b) elastic angle change ϕ_e [rad]



(c) plastic angle change ϕ_p [rad]

Figure 15: Twisting of a textile band: (a) shear stress, (b) elastic angle change and (c) plastic angle change before twisting, at twisting angle 240° and after untwisting (left to right). The green lines illustrate the two considered fiber families.

9 Conclusion

We have presented a nonlinear shear elastoplasticity model for dry textile fabrics within the theoretical framework of [Duong et al. \(2023\)](#) that is based on general anisotropic Kirchhoff-Love shells with embedded fibers. Therefore the change of the fiber angle – the angle between two fiber families – is split into elastic and plastic parts. It is shown that these angle changes can be induced from strain tensors of the displacement gradient. With this, a yield function with isotropic hardening is proposed based on the observed experimental data of [Cao et al. \(2008\)](#). The yield function uses seven parameters to capture the three phases occurring in the rotational inter-ply friction between fiber families: initial sticking, rotational sliding friction with low plastic resistance, and increased hardening due to yarn-yarn locking. The elastoplasticity formulation is solved by a predictor-corrector algorithm, which is then implemented within the isogeometric Kirchhoff-Love shell formulation of [Duong et al. \(2022\)](#). In order to verify the finite element implementation, the analytical solution of the picture frame test is presented for the proposed elastoplasticity model. The analytical solution captures multiple loading and unloading cycles by accounting for the expanding yield surface.

The proposed plasticity model is calibrated from the picture from test and validated by the bias extension test for six different samples sizes. It is observed that the proposed model consistently predicts the experiment data, especially during the sticking and rotational sliding phase. In the increased hardening phase, where the experiment data becomes more scattered across different sources, our model prediction curves lie between the mean values of the experiment data.

A Angle measures as invariants induced from strain tensors

This section shows that the angle strain measures (33)-(35) can be induced from strain tensors. To this end, similarly to Eq. (37), we extract the part of deformation gradient (17) that excludes the change in fiber lengths at current configuration \mathcal{S} . I.e.

$$\bar{\mathbf{F}} := \sum_{i=1}^2 \mathbf{F}(\mathbf{L}_i \otimes \mathbf{L}^i) \lambda_i^{-1} = \boldsymbol{\ell}_i \otimes \mathbf{L}^i . \quad (100)$$

The corresponding right Cauchy-Green surface tensors following from Eq. (100) and (37) are

$$\bar{\mathbf{C}} := \bar{\mathbf{F}}^T \bar{\mathbf{F}} = \bar{a}_{\alpha\beta} \mathbf{A}^\alpha \otimes \mathbf{A}^\beta = \theta_{ij} \mathbf{L}^i \otimes \mathbf{L}^j , \quad (101)$$

$$\mathbf{C}_p := \mathbf{F}_p^T \mathbf{F}_p = \hat{a}_{\alpha\beta} \mathbf{A}^\alpha \otimes \mathbf{A}^\beta = \hat{\theta}_{ij} \mathbf{L}^i \otimes \mathbf{L}^j , \quad (102)$$

where θ_{ij} and $\hat{\theta}_{ij}$ are defined by Eq. (29) and (30), respectively, and where $\bar{a}_{\alpha\beta}$ and $\hat{a}_{\alpha\beta}$ are the components of tensors $\bar{\mathbf{C}}$ and \mathbf{C}_p , respectively, with respect to base $\mathbf{A}^\alpha \otimes \mathbf{A}^\beta$ in the reference configuration. From Eq. (101) and (102), they can be expressed in terms of the fiber angles as

$$\begin{aligned} \bar{a}_{\alpha\beta} &= \mathbf{A}_\alpha \bar{\mathbf{C}} \mathbf{A}_\beta = L_{\alpha\beta}^{ij} \theta_{ij}, \\ \hat{a}_{\alpha\beta} &= \mathbf{A}_\alpha \mathbf{C}_p \mathbf{A}_\beta = L_{\alpha\beta}^{ij} \hat{\theta}_{ij} , \end{aligned} \quad (103)$$

where $L_{\alpha\beta}^{ij} := (\mathbf{L}^j \otimes \mathbf{L}^j) : (\mathbf{A}_\alpha \otimes \mathbf{A}_\beta)$ denote the curvilinear components of structural fiber tensors $\mathbf{L}^j \otimes \mathbf{L}^j$ in the reference configuration. Note that, fiber family index i and curvilinear coordinate index α can be raised or lowered by its corresponding metrics, e.g. $L_{ij}^{\alpha\beta} = \Theta_{ik} \Theta_{lj} L_{\gamma\delta}^{k\ell} A^{\alpha\gamma} A^{\delta\beta}$.

Also following from Eq. (101) and (102), we find that angle measures (33)-(35) can be expressed as

$$\phi = \mathbf{L}_1 (\bar{\mathbf{C}} - \mathbf{I}) \mathbf{L}_2 = L_{12}^{\alpha\beta} (\bar{a}_{\alpha\beta} - A_{\alpha\beta}) , \quad (104)$$

$$\phi_e = \mathbf{L}_1 (\bar{\mathbf{C}} - \mathbf{C}_p) \mathbf{L}_2 = L_{12}^{\alpha\beta} (\bar{a}_{\alpha\beta} - \hat{a}_{\alpha\beta}) , \quad (105)$$

$$\phi_p = \mathbf{L}_1 (\mathbf{C}_p - \mathbf{I}) \mathbf{L}_2 = L_{12}^{\alpha\beta} (\hat{a}_{\alpha\beta} - A_{\alpha\beta}) , \quad (106)$$

i.e. they are invariants of strain measures $\bar{\mathbf{C}} - \mathbf{I}$, $\bar{\mathbf{C}} - \mathbf{C}_p$ and $\mathbf{C}_p - \mathbf{I}$, respectively.

Remark A.1: It can be verified that deformations characterized by (37) and (100), preserve the length of fiber i in configurations $\hat{\mathcal{S}}$ and \mathcal{S} , respectively. Indeed

$$(\mathbf{F}_p \mathbf{L}_i) \cdot (\mathbf{F}_p \mathbf{L}_i) = \mathbf{L}_i \mathbf{C}_p \mathbf{L}_i = \hat{\theta}_{ii} = \hat{\boldsymbol{\ell}}_i \cdot \hat{\boldsymbol{\ell}}_i = 1 , \quad (107)$$

$$(\bar{\mathbf{F}} \mathbf{L}_i) \cdot (\bar{\mathbf{F}} \mathbf{L}_i) = \mathbf{L}_i \bar{\mathbf{C}} \mathbf{L}_i = \theta_{ii} = \boldsymbol{\ell}_i \cdot \boldsymbol{\ell}_i = 1 , \quad (108)$$

where Eqs. (30) and (31) have been used, and no summation is applied on index i .

Remark A.2: As the consequence of this length preservation in configuration $\hat{\mathcal{S}}$, the surface area changes during plastic deformation (i.e. $J_p \neq 1$).

Remark A.3: A material model based on invariants (104)-(106) induces only the effective membrane stress (60.1) that contributes to the first term of Eq. (46.2). Indeed, in view of Eqs. (102), (101), (100), (39) and (26), we can conclude that tensors $\bar{\mathbf{C}}$ and \mathbf{C}_p are only associated with the first displacement gradient, which does not affect curvature tensors (21) and (22). Invariants of this types usually facilitate the decomposition of stretching and bending, which is beneficial in the construction of shell material models.

B Analytical solution of angle plasticity in the picture frame test

This section presents the analytical solution for the picture frame test shown in Fig. 3a-b. A textile fabric is mounted in a square frame (Fig. 3a), which is then deformed into a rhombus (Fig. 3b). The aim is to find an analytical expression for the stress based on the angle plasticity model proposed in Sec. 5. Our solution is applicable to multiple loading (or unloading) cycles. To this end, we employ a so-called expanding yield surface approach: It solves for the shear stress within a given loading or unloading interval using the initial conditions provided from the solution at the end of the previous interval.

B.1 Various angle measures in the picture frame test

The initial configuration and fiber directions in the picture frame test are seen in Fig. 3a. In this case the angle measures from Eq. (29) and (31) become

$$\Theta_{12} := \mathbf{L}_1 \cdot \mathbf{L}_1 = \cos \Theta = 0 , \quad (109)$$

$$\theta_{12} := \boldsymbol{\ell}_1 \cdot \boldsymbol{\ell}_2 = \cos \theta . \quad (110)$$

For the plotting of the testing results, it is convenient to use the shear angle

$$\gamma := 90^\circ - \theta \quad [\text{deg}] . \quad (111)$$

Consider a loading (or unloading) interval, denoted \mathcal{C} , where $\theta_{12} \in [\theta_{12}^0, \theta_{12}^{\max}]$. We define the relative angles $\bar{\phi}$ similarly to Eq. (33)-(35) but now with respect to the configuration at the start of interval \mathcal{C} . Here, the bar indicates an interval-wise quantity. This means that within interval $[\theta_{12}^0, \theta_{12}^{\max}]$ the configuration at θ_{12} is identical to the current configuration \mathcal{S} . But the configuration at θ_{12}^0 now becomes the reference configuration and is denoted by $\bar{\mathcal{S}}_0$. Between $\bar{\mathcal{S}}_0$ and \mathcal{S} , the intermediate configuration is denoted by $\bar{\mathcal{S}}$ – generally different from $\hat{\mathcal{S}}$. The fiber directions on configurations $\bar{\mathcal{S}}_0$ and $\bar{\mathcal{S}}$ are denoted by $\bar{\ell}_i^0$ and $\bar{\ell}_i$, respectively. Similarly to Eqs. (29) and (30), fiber directions $\bar{\ell}_i^0$ and $\bar{\ell}_i$ constitute the relative fiber angles, denoted θ_{12}^0 and $\bar{\theta}_{12}$, respectively.

With these, the relative angles within interval \mathcal{C} are defined as

$$\bar{\phi} := \theta_{12} - \theta_{12}^0, \quad (112)$$

$$\bar{\phi}_e := \theta_{12} - \bar{\theta}_{12}, \quad (113)$$

$$\bar{\phi}_p := \bar{\phi} - \bar{\phi}_e. \quad (114)$$

Consequently $\bar{\phi}$ always ranges from zero to $\phi^{\max} := \theta_{12}^{\max} - \theta_{12}^0$. Note that ϕ^{\max} can take a negative value.

B.2 Shear stress in a loading interval

Similar to the interval-wise angle measures defined in Eq. (112)-(114), the shear stress can be expressed in an interval-wise manner as follows.

Consider a loading or unloading interval \mathcal{C} , which proceeds from the previous interval, say \mathcal{C}^0 . Given that $\bar{\phi}$ ranges from 0 to ϕ^{\max} and the fabric deforms from elastic phase \mathcal{C}_e to plastic phase \mathcal{C}_p , the total shear stress τ can be computed from the shear stress at the end of interval \mathcal{C}^0 plus an additional stress. That is,

$$\tau = \tau^0 + \bar{\tau}, \quad (115)$$

where τ^0 and $\bar{\tau}$ denote the shear stress due to the change of fiber angles in interval \mathcal{C}^0 and \mathcal{C} , respectively. Here, $\bar{\tau}$ follows from (72) with (114) as

$$\bar{\tau} := \mu_f \bar{\phi}_e = \mu_f (\bar{\phi} - \bar{\phi}_p). \quad (116)$$

Here, the internal variable $\bar{\phi}_p$ is still unknown and can be solved by the following approach, which we term the *expanding yield surface approach*.

B.3 Analytical solution by an *expanding yield surface approach*

We now aim at solving for $\bar{\phi}_p$ to compute shear stress $\bar{\tau}$. To this end, performing time integration over plastic phase \mathcal{C}_p on both sides of the evolution equations (78) and (79) gives

$$h(\bar{\phi}_p + c_1) = \lambda + c_2, \quad (117)$$

$$Q := \lambda + c_2 = q + c_3, \quad (118)$$

where $\bar{\phi}_p$ is the plastic angle defined in Eq. (114), Q denotes the integration (i.e. accumulation) of q (and also λ) over \mathcal{C} , and parameters c_1 , c_2 , and c_3 are constants to be determined from the

initial conditions, see Eq. (129). Inserting Eq. (117) into (118) gives the explicit expression of the hardening variable q in terms of $\bar{\phi}_p$ as⁷

$$q = \lambda + c_2 - c_3 = h(\bar{\phi}_p + c_1) - c_3 =: \tilde{q}(\bar{\phi}_p) . \quad (119)$$

With this and angle $\bar{\phi}$ given, we can solve for $\bar{\phi}_p$

$$f_y(\tau, \tilde{q}) = 0 \quad (120)$$

in a plastic state. Here,

$$f_y = \bar{\tau} h - (\tau_y + |\tau^0|) - A \operatorname{asinh}(a \tilde{q}) - B \tanh(b \tilde{q}) - C \tilde{q}^c \quad (121)$$

follows from (76) when inserting (115), and $\bar{\tau}$ is expressed by Eq. (116) with (119). Therefore, f_y from Eq. (121) becomes a function of sole (scalar) variable $\bar{\phi}_p$, and Eq. (120) can be solved for $\bar{\phi}_p$ by Newton's method using the derivative

$$f'_y = -h \mu_f - \frac{A a h}{\sqrt{1 + a^2 \tilde{q}^2}} - B b h \operatorname{sech}^2(b \tilde{q}) - C c h \tilde{q}^{c-1} . \quad (122)$$

As seen from Eq. (121), the yield stress is shifted by $|\tau^0|$ since the current interval starts from the last point of the previous interval. In other words, the yield function expands by $|\tau^0|$.

Further, the elastic phase in interval \mathcal{C} can be defined from function (121) with the condition

$$f_y(\bar{\tau}) < 0 . \quad (123)$$

Note that in this phase, hardening variable \tilde{q} does not evolve. That is, it remains constant at the value from the previous loading interval, say $\tilde{q} = q_0$, and $\bar{\tau} = \mu_f \bar{\phi}$ from Eq. (116) since $\bar{\phi}_p = 0$, and function (121) becomes

$$f_y = \mu_f |\bar{\phi}| - (\tau_y + |\tau^0|) - A \operatorname{asinh}(a q_0) - B \tanh(b q_0) - C q_0^c . \quad (124)$$

With this, condition (123) gives the definition of the elastic zone as

$$|\bar{\phi}| < \phi_y , \quad (125)$$

where we have defined the so-called yield angle ϕ_y as

$$\phi_y := \frac{1}{\mu_f} \left[\tau_y + |\tau^0| + A \operatorname{asinh}(a q_0) + B \tanh(b q_0) + C q_0^c \right] . \quad (126)$$

In particular for the initial loading interval, setting $\tau^0 = 0$, and $q_0 = 0$ in Eq. (126) gives $\phi_y = \tau_y / \mu_f$.

B.4 Analytical solution procedure

At the start of interval \mathcal{C} , the values of shear stress τ , accumulated plastic angle λ , hardening variable q , and accumulation Q in Eq. (118) are taken over from (the end of) the previous interval \mathcal{C}_0 as

$$\begin{aligned} \tau &= \tau^0 , \\ \lambda &= \lambda^0 , \\ q &= q^0 \\ Q &= Q^0 , \end{aligned} \quad (127)$$

⁷Here we keep the constants separate for the sake of comparison with the general numerical procedure in Sec. 5.2. Alternatively, one can combine the constants and eliminate variable λ .

where $Q^0 = \tau^0 = \lambda^0 = \tau^0 = q^0 = 0$ for the initial loading interval. With this, we can compute the yield angle ϕ_y from Eq. (126).

For any given $\bar{\phi} \in [0, \phi^{\max}]$, if $\bar{\phi}$ falls in the elastic phase \mathcal{C}_e , i.e. $|\bar{\phi}| \leq \phi_y$, the shear stress (115) becomes

$$\tau = \tau^0 + \mu_f \bar{\phi}, \quad (128)$$

since $\bar{\phi}_p = 0$.

On the other hand, if $\bar{\phi}$ falls in the plastic phase \mathcal{C}_p , i.e. $|\bar{\phi}| > \phi_y$, we compute $\bar{\phi}_p$ by solving Eq. (120) with f_y defined by Eq. (121), where the three constants appearing in Eq. (117) and (118) are determined from the initial conditions at the start of plastic phase \mathcal{C}_p . This gives

$$\begin{aligned} c_3 &= Q^0 - q^0, \\ c_2 &= Q^0 - \lambda^0, \\ c_1 &= h^e Q^0, \\ h^e &= \text{sign } \tau_e. \end{aligned} \quad (129)$$

Here, τ_e denotes the shear stress (128) at the end of the elastic phase \mathcal{C}_e (i.e. the start of plastic phase \mathcal{C}_p), and we have used the condition $\bar{\phi}_p = 0$ at the start of plastic phase \mathcal{C}_p , and the fact that Q , q , and λ remain unchanged in \mathcal{C}_e as p and λ evolve only in plastic phases.

With $\bar{\phi}_p$ computed, apart from stress τ from (115), variables q , Q and λ from Eq. (119) and (117) can be computed at the end of the current interval, so that they are available for the initial conditions of the next loading interval.

Acknowledgments

The funding of the German Research Foundation (DFG) through project SA1822/11-1 is gratefully acknowledged. Thang X. Duong thanks Prof. Josef Kiendl for his support.

References

- Aimène, Y., Vidal-Sallé, E., Hagège, B., Sidoroff, F., and Boisse, P. (2010). A hyperelastic approach for composite reinforcement large deformation analysis. *J. Compos. Mater.*, **44**(1):5–26.
- Alaydin, M., Benson, D., and Bazilevs, Y. (2021). An updated Lagrangian framework for isogeometric Kirchhoff–Love thin-shell analysis. *Comput. Methods Appl. Mech. Engrg.*, **384**:113977.
- Allaoui, S., Hivet, G., Wendling, A., Ouagne, P., and Soulat, D. (2012). Influence of the dry woven fabrics meso-structure on fabric/fabric contact behavior. *J. Compos. Mater.*, **46**(6):627–639.
- Ambati, M., Kiendl, J., and De Lorenzis, L. (2018). Isogeometric Kirchhoff–Love shell formulation for elasto-plasticity. *Comput. Methods Appl. Mech. Engrg.*, **340**:320–339.
- Asmanoglo, T. and Menzel, A. (2017). A multi-field finite element approach for the modelling of fibre-reinforced composites with fibre-bending stiffness. *Comput. Methods Appl. Mech. Engrg.*, **317**:1037–1067.

- Auddya, D., Zhang, X., Gulati, R., Vasani, R., Garikipati, K., Rangamani, P., and Rudraraju, S. (2021). Biomembranes undergo complex, non-axisymmetric deformations governed by Kirchhoff–Love kinematics and revealed by a three-dimensional computational framework. *Proc. R. Soc. A: Math. Phys. Eng. Sci.*, **477**(2255):20210246.
- Balobanov, V., Kiendl, J., Khakalo, S., and Niiranen, J. (2019). Kirchhoff–Love shells within strain gradient elasticity: Weak and strong formulations and an H3-conforming isogeometric implementation. *Comput. Methods Appl. Mech. Engrg.*, **344**:837–857.
- Barbagallo, G., Madeo, A., Azehaf, I., Giorgio, I., Morestin, F., and Boisse, P. (2017). Bias extension test on an unbalanced woven composite reinforcement: Experiments and modeling via a second-gradient continuum approach. *J. Compos. Mater.*, **51**(2):153–170.
- Boisse, P., Hamila, N., Guzman-Maldonado, E., Madeo, A., Hivet, G., and Dell’Isola, F. (2017). The bias-extension test for the analysis of in-plane shear properties of textile composite reinforcements and prepregs: a review. *Int. J. Mater. Form.*, **10**:473–492.
- Borden, M. J., Scott, M. A., Evans, J. A., and Hughes, T. J. R. (2011). Isogeometric finite element data structures based on Bezier extraction of NURBS. *Int. J. Numer. Meth. Engrg.*, **87**:15–47.
- Brank, B., Perić, D., and Damjanić, F. (1997). On large deformations of thin elasto-plastic shells: implementation of a finite rotation model for quadrilateral shell elemen. *Int. J. Numer. Meth. Engrg.*, **40**(4):689–726.
- Bussetta, P. and Correia, N. (2018). Numerical forming of continuous fibre reinforced composite material: A review. *Compos. - A: Appl. Sci. Manuf.*, **113**:12–31.
- Canham, P. B. (1970). The minimum energy of bending as a possible explanation of the biconcave shape of the human red blood cell. *J. Theoret. Biol.*, **26**:61–81.
- Cao, J., Akkerman, R., Boisse, P., Chen, J., Cheng, H. S., de Graaf, E. F., Gorczyca, J. L., Harrison, P., Hivet, G., Launay, J., Lee, W., Liu, L., Lomov, S. V., Long, A., de Luycker, E., Morestin, F., Padvoiskis, J., Peng, X. Q., Sherwood, J., Stoilova, T., Tao, X. M., Verpoest, I., Willems, A., Wiggers, J., Yu, T. X., and Zhu, B. (2008). Characterization of mechanical behavior of woven fabrics: Experimental methods and benchmark results. *Compos. Part A Appl. Sci. Manuf.*, **39**(6):1037–1053.
- Charmetant, A., Orliac, J., Vidal-Sallé, E., and Boisse, P. (2012). Hyperelastic model for large deformation analyses of 3d interlock composite preforms. *Compos. Sci. Technol.*, **72**(12):1352–1360.
- Coleman, B. D. and Noll, W. (1964). The thermodynamics of elastic materials with heat conduction and viscosity. *Arch. Ration. Mech. Anal.*, **13**:167–178.
- Cortivo, N. D., Felippa, C. A., Bavestrello, H., and Silva, W. T. (2009). Plastic buckling and collapse of thin shell structures, using layered plastic modeling and co-rotational andes finite elements. *Comput. Methods Appl. Mech. Engrg.*, **198**(5):785–798.
- dell’Isola, F. and Steigmann, D. (2015). A two-dimensional gradient-elasticity theory for woven fabrics. *J. Elast.*, **118**:113–125.
- Denis, Y., Guzman-Maldonado, E., Hamila, N., Colmars, J., and Morestin, F. (2018). A dissipative constitutive model for woven composite fabric under large strain. *Compos. - A: Appl. Sci. Manuf.*, **105**:165–179.

- Dujc, J. and Brank, B. (2012). Stress resultant plasticity for shells revisited. *Comput. Methods Appl. Mech. Engrg.*, **247-248**:146–165.
- Duong, T. X., Itskov, M., and Sauer, R. A. (2022). A general isogeometric finite element formulation for rotation-free shells with in-plane bending of embedded fibers. *Int. J. Numer. Meth. Engrg.*, **123**(14):3115–3147.
- Duong, T. X., Itskov, M., and Sauer, R. A. (2024). Response to David Steigmann’s discussion of our paper. *Math. Mech. Solids*, **29**(5):1038–1044.
- Duong, T. X., Khiêm, V. N., Itskov, M., and Sauer, R. A. (2023). A general theory for anisotropic Kirchhoff–Love shells with in-plane bending of embedded fibers. *Math. Mech. Solids*, **28**:1274–1317.
- Duong, T. X., Roohbakhshan, F., and Sauer, R. A. (2017). A new rotation-free isogeometric thin shell formulation and a corresponding continuity constraint for patch boundaries. *Comput. Methods Appl. Mech. Engrg.*, **316**:43–83.
- Ferretti, M., Madeo, A., Dell’Isola, F., and Boisse, P. (2014). Modeling the onset of shear boundary layers in fibrous composite reinforcements by second-gradient theory. *Z. fur Angew. Math. Phys.*, **65**:587–612.
- Ghaffari, R., Duong, T. X., and Sauer, R. A. (2018). A new shell formulation for graphene structures based on existing ab-initio data. *Int. J. Solids Struct.*, **135**:37–60.
- Helfrich, W. (1973). Elastic properties of lipid bilayers: Theory and possible experiments. *Z. Naturforsch.*, **28c**:693–703.
- Hughes, T. J. R., Cottrell, J. A., and Bazilevs, Y. (2005). Isogeometric analysis: CAD, finite elements, NURBS, exact geometry and mesh refinement. *Comput. Methods Appl. Mech. Engrg.*, **194**:4135–4195.
- Huynh, G., Zhuang, X., Bui, H., Meschke, G., and Nguyen-Xuan, H. (2020). Elasto-plastic large deformation analysis of multi-patch thin shells by isogeometric approach. *Finite Elem. Anal. Des.*, **173**:103389.
- Khiêm, V. N. and Itskov, M. (2016). Analytical network-averaging of the tube model: Rubber elasticity. *J. Mech. Phys. Solids*, **95**:254–269.
- Khiêm, V. N., Jabareen, M., Poudel, R., Tang, X., and Itskov, M. (2024). Modeling of textile composite using analytical network-averaging and gradient damage approach. *J. Mech. Phys. Solids*, **193**:105874.
- Khiêm, V. N., Krieger, H., Itskov, M., Gries, T., and Stapleton, S. E. (2018). An averaging based hyperelastic modeling and experimental analysis of non-crimp fabrics. *Int. J. Solids Struct.*, **154**:43–54.
- Kiendl, J., Bletzinger, K.-U., Linhard, J., and Wüchner, R. (2009). Isogeometric shell analysis with Kirchhoff–Love elements. *Comput. Methods Appl. Mech. Engrg.*, **198**:3902–3914.
- Kiendl, J., Hsu, M.-C., Wu, M. C., and Reali, A. (2015). Isogeometric Kirchhoff–Love shell formulations for general hyperelastic materials. *Comput. Methods Appl. Mech. Engrg.*, **291**:280–303.
- Kim, K. and Lomboy, G. (2006). A co-rotational quasi-conforming 4-node resultant shell element for large deformation elasto-plastic analysis. *Comput. Methods Appl. Mech. Engrg.*, **195**(44):6502–6522.

- Li, J., Hamila, N., Guzman-Maldonado, E., L’Hostis, G., and Wang, P. (2023). Improved hyperelastic model for simulating the forming of biaxial braided fabrics. *Compos. Struct.*, **321**:117263.
- Liu, N., Hsu, M.-C., Lua, J., and Phan, N. (2022). A large deformation isogeometric continuum shell formulation incorporating finite strain elastoplasticity. *Comput. Mech.*, **70**:965–976.
- Lu, Q., Arroyo, M., and Huang, R. (2009). Elastic bending modulus of monolayer graphene. *J. Phys. D Appl. Phys.*, **42**(10):102002.
- Madeo, A., Barbagallo, G., D’Agostino, M. V., and Boisse, P. (2016). Continuum and discrete models for unbalanced woven fabrics. *Int. J. Solids Struct.*, **94-95**:263–284.
- Magisano, D. and Corrado, A. (2023). New robust and efficient global iterations for large deformation finite element analysis of beams and shells with material nonlinearity. *Comput. Methods Appl. Mech. Engrg.*, **406**:115900.
- Melnik, A. V., Luo, X., and Ogden, R. W. (2018). A generalised structure tensor model for the mixed invariant i_8 . *Int. J. Non-Linear Mech.*, **107**:137–148.
- Mokhalingam, A., Gupta, S. S., and Sauer, R. A. (2024). Continuum contact model for friction between graphene sheets that accounts for surface anisotropy and curvature. *Phys. Rev. B*, **109**:035435.
- Paul, K., Zimmermann, C., Duong, T. X., and Sauer, R. A. (2020). Isogeometric continuity constraints for multi-patch shells governed by fourth-order deformation and phase field models. *Comput. Methods Appl. Mech. Engrg.*, **370**:113219.
- Peng, X. and Cao, J. (2005). A continuum mechanics-based non-orthogonal constitutive model for woven composite fabrics. *Compos. - A: Appl. Sci. Manuf.*, **36**(6):859–874.
- Peng, X., Guo, Z., Du, T., and Yu, W.-R. (2013). A simple anisotropic hyperelastic constitutive model for textile fabrics with application to forming simulation. *Compos. B: Eng.*, **52**:275–281.
- Quenzel, P., Kröger, H., Manin, B., Vu, K. N., Duong, T. X., Gries, T., Itskov, M., and Sauer, R. A. (2022). Material characterisation of biaxial glass-fibre non-crimp fabrics as a function of ply orientation, stitch pattern, stitch length and stitch tension. *J. Compos. Mater.*, **56**(26):3971–3991.
- Rivlin, R. S. and Rideal, E. K. (1949). Large elastic deformations of isotropic materials vi. further results in the theory of torsion, shear and flexure. *Philos. Trans. R. Soc. London. Ser. A*, **242**(845):173–195.
- Roohbakhshan, F. and Sauer, R. A. (2017). Efficient isogeometric thin shell formulations for soft biological materials. *Biomech. Model. Mechanobiol.*, **16**:1569–1597.
- Rubin, M. B. and Jabareen, M. (2008). Physically based invariants for nonlinear elastic orthotropic solids. *J. Elast.*, **90**:1–18.
- Sansour, C. and Wagner, W. (2001). A model of finite strain viscoplasticity based on unified constitutive equations. theoretical and computational considerations with applications to shells. *Comput. Methods Appl. Mech. Engrg.*, **191**(3):423–450.
- Sauer, R. A. and Duong, T. X. (2017). On the theoretical foundations of solid and liquid shells. *Math. Mech. Solids*, **22**:343–371.

- Sauer, R. A., Duong, T. X., and Corbett, C. J. (2014). A computational formulation for constrained solid and liquid membranes considering isogeometric finite elements. *Comput. Methods Appl. Mech. Engrg.*, **271**:48–68.
- Sauer, R. A., Duong, T. X., Mandadapu, K. K., and Steigmann, D. J. (2017). A stabilized finite element formulation for liquid shells and its application to lipid bilayers. *J. Comput. Phys.*, **330**:436–466.
- Sauer, R. A., Ghaffari, R., and Gupta, A. (2019). The multiplicative deformation split for shells with application to growth, chemical swelling, thermoelasticity, viscoelasticity and elastoplasticity. *Int. J. Solids Struct.*, **174-175**:53–68.
- Schäfer, B., Därr, D., Zheng, R., Naouar, N., and Kärger, L. (2024). A hyperelastic approach for modeling the membrane behavior in finite element forming simulation of unidirectional non-crimp fabrics (UD-NCF). *Compos. - A: Appl. Sci. Manuf.*, **185**:108359.
- Schäfer, F., Werner, H. O., Henning, F., and Kärger, L. (2023). A hyperelastic material model considering biaxial coupling of tension–compression and shear for the forming simulation of woven fabrics. *Compos. - A: Appl. Sci. Manuf.*, **165**:107323.
- Schieck, B., Smoleński, W., and Stumpf, H. (1999). A shell finite element for large strain elastoplasticity with anisotropies: Part I: Shell theory and variational principle. *Int. J. Solids Struct.*, **36**(35):5399–5424.
- Schulte, J., Dittmann, M., Eugster, S. R., Hesch, S., Reinicke, T., Dell’Isola, F., and Hesch, C. (2020). Isogeometric analysis of fiber reinforced composites using Kirchhoff-Love shell elements. *Comput. Methods Appl. Mech. Engrg.*, **362**:112845.
- Shapiro, G. (1961). On yield surfaces for ideally plastic shells. In *Problems of Continuum Mechanics*, volume **414**, Philadelphia, PA. SIAM Press.
- Simo, J. and Fox, D. (1989). On a stress resultant geometrically exact shell model. Part I: Formulation and optimal parametrization. *Comput. Methods Appl. Mech. Engrg.*, **72**(3):267–304.
- Simo, J. and Kennedy, J. (1992). On a stress resultant geometrically exact shell model. part v. nonlinear plasticity: formulation and integration algorithms. *Comput. Methods Appl. Mech. Engrg.*, **96**(2):133–171.
- Simo, J. C. and Hughes, T. J. (2006). *Computational inelasticity*, volume **7**. Springer Science & Business Media.
- Skallerud, B. and Haugen, B. (1999). Collapse of thin shell structures-stress resultant plasticity modelling within a co-rotated andes finite element formulation. *Int. J. Numer. Meth. Engrg.*, **46**(12):1961 – 1986.
- Skallerud, B., Myklebust, L., and Haugen, B. (2001). Nonlinear response of shell structures: effects of plasticity modelling and large rotations. *Thin-Walled Struct.*, **39**(6):463–482.
- Spencer, A. J. M. (1984). *Constitutive Theory for Strongly Anisotropic Solids*, pages 1–32. Springer Vienna, Vienna.
- Spencer, A. J. M. and Soldatos, K. P. (2007). Finite deformations of fibre-reinforced elastic solids with fibre bending stiffness. *Int. J. Nonlin. Mech.*, **42**(2):355–368.
- Stanley, G. M. (1985). *Continuum-based shell elements*. Stanford University.

- Steigmann, D. J. (2012). Theory of elastic solids reinforced with fibers resistant to extension, flexure and twist. *Int. J. Nonlin. Mech.*, **47**(7):734–742.
- Steigmann, D. J. (2018). Equilibrium of elastic lattice shells. *J. Eng. Math*, **109**:47–61.
- Tepole, A. B., Kabaria, H., Bletzinger, K.-U., and Kuhl, E. (2015). Isogeometric Kirchhoff–Love shell formulations for biological membranes. *Comput. Methods Appl. Mech. Engrg.*, **293**:328–347.
- Vu-Bac, N., Duong, T. X., Lahmer, T., Areias, P., Sauer, R. A., Park, H. S., and Rabczuk, T. (2019). A NURBS-based inverse analysis of thermal expansion induced morphing of thin shells. *Comput. Methods Appl. Mech. Engrg.*, **350**:480–510.
- Wagner, W. and Gruttmann, F. (2005). A robust non-linear mixed hybrid quadrilateral shell element. *Int. J. Numer. Meth. Engrg.*, **64**(5):635–666.
- Witt, C., Kaiser, T., and Menzel, A. (2021). A finite deformation isogeometric finite element approach to fibre-reinforced composites with fibre bending stiffness. *J. Eng. Math.*, **128**(1):15.
- Zeng, Q., Combescure, A., and Arnaudeau, F. (2001). An efficient plasticity algorithm for shell elements application to metal forming simulation. *Comput. Struct.*, **79**(16):1525–1540.
- Zimmerberg, J. and Kozlov, M. M. (2006). How proteins produce cellular membrane curvature. *Nat. Rev. Mol. Cell Biol.*, **7**(1):9–19.
- Zimmermann, C., Toshniwal, D., Landis, C. M., Hughes, T. J., Mandadapu, K. K., and Sauer, R. A. (2019). An isogeometric finite element formulation for phase transitions on deforming surfaces. *Comput. Methods Appl. Mech. Engrg.*, **351**:441–477.